Numerical optimization and analysis of solid-state battery cathode hetero-agglomerate formation in turbulent pipe flows

Victor Kolck[1,*], Joscha Witte[2], Lukas Fuchs[3], Finn Frankenberg[4], Arno Kwade[4], Volker Schmidt[3], Eberhard Schmidt[2], Harald Kruggel-Emden[1]

[1]Technische Universität Berlin, Chair of Mechanical Process Engineering and Solids Processing, Ernst-Reuter-Platz 1, D-10587 Berlin, Germany.

[2]University of Wuppertal, Institute of Particle Technology, Rainer-Gruenter-Str. Geb. FF, D-42119 Wuppertal, Germany.

[3]Ulm University, Institute of Stochastics, Helmholtzstr. 18, D-89069 Ulm, Germany.

[4]Technische Universität Braunschweig, Institute for Particle Technology, Volkmaroder Straße 5, D-38104 Braunschweig, Germany.

Email corresponding author: kolck@tu-berlin.de

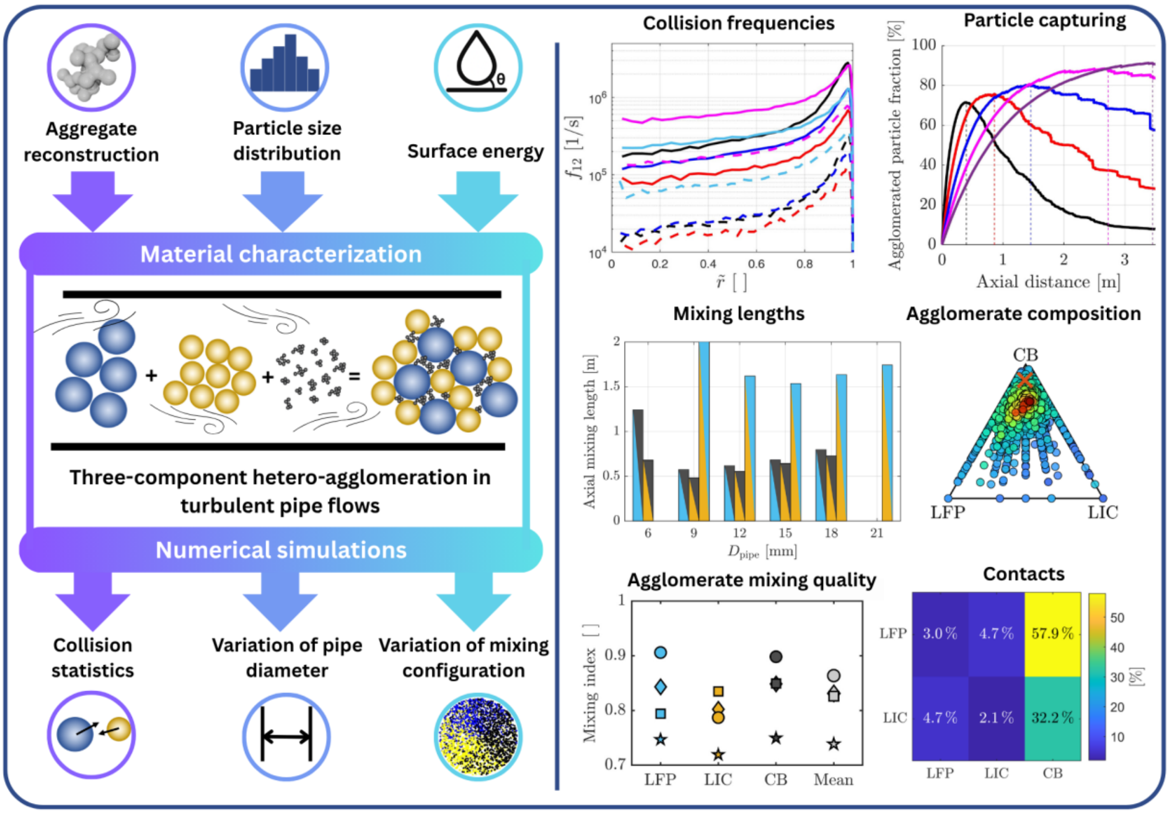

Abstract

Hetero-agglomeration of micron- and submicron-sized particles enables the formation of all-solid-state battery cathode materials with enhanced safety and energy density. This study investigates a turbulent pipe flow process for mixing lithium iron phosphate ($LiFePO_4$, LFP), lithium indium chloride (Li_3InCl_6, LIC), and carbon black (CB) to form three-component hetero-agglomerates. The analysis aims to identify suitable pipe dimensions and evaluate how different mixing configurations affect agglomerate size, composition, and structure. The investigation employs a dedicated simulation framework utilizing a mesh-free representation of turbulent flow fields derived from direct numerical simulation datasets. Lagrangian particle tracking incorporates an improved discrete random walk model, while stochastic agglomerate structure simulations account for various turbulent collision mechanisms, hydrodynamic interactions, and breakup events. Prior to simulations, virtual CB aggregates were stereologically reconstructed from scanning electron microscopy images, the particle size distributions were determined using laser light diffraction, and the surface energies of all materials were determined from contact angle measurements using the Owens-Wendt-Rabel-Kaelble method. Simulations examined parallel mixing and sequential premixing configurations (LFP-CB, LIC-CB, and LFP-LIC) across various pipe diameters. For parallel mixing under experimental process conditions, an 18 mm pipe diameter proves optimal, maximizing particle capture in agglomerates at 2.73 m. Each premixing combination exhibits a distinct optimal diameter, minimizing deposition while enabling short mixing lengths. The mixing configuration significantly influenced the agglomerate composition, the material-specific mixing quality measures and the contact-pair distribution. The findings provide concrete recommendations for experimental process design regarding pipe dimensions and mixing strategies, while the influence on electrochemical properties requires further investigation.

Keywords: Hetero-agglomeration; Turbulent pipe flow; Agglomerate structure; Particle mixing; Solid-state batteries; Owens-Wendt-Rabel-Kaelble method; Stereological calibration

1 Introduction

The mixing of particulate systems represents a fundamental unit operation in process engineering, with applications across diverse industries such as pharmaceuticals, chemicals, and materials science (Jin and Shen, 2024). Hetero-agglomeration, the specific combination of particles of different materials, can result in unique and enhanced properties of the composite due to the formation of hetero-contacts at the interfaces of the particles (Kolck et al., 2026, 2023a; Witte et al., 2023). These hetero-contacts facilitate interactions such as charge, heat, or mass transfer without necessitating chemical reactions between the components. The structural arrangement of the particles within these hetero-agglomerates is of paramount importance, as it determines the quantity of resulting hetero-contacts and influences the characteristics of the resultant material.

In the context of energy storage, hetero-agglomeration plays a critical role in the development of advanced battery materials, particularly for all-solid-state batteries (ASSBs). Unlike conventional lithium-ion batteries, which use a liquid electrolyte, ASSBs incorporate a solid electrolyte, offering benefits such as improved safety and increased energy density (Janek and Zeier, 2016; Jung et al., 2015; Kerman et al., 2017). The cathode of an ASSB is a complex composite consisting of cathode active material (CAM, Fig. 1 a)) particles, solid electrolyte (SE, Fig. 1 b)) particles, and conductive additives such as carbon black (CB, Fig. 1 c)) (Frankenberg et al., 2025; Kissel et al., 2026a). The distribution and interaction of these components through hetero-contacts significantly influence the battery's electrochemical performance (Wang et al., 2012). Despite the promising potential of these materials, the relationship between the structural arrangement of the hetero-agglomerates, the cathode material consist of, and the resulting battery performance remains inadequately understood (Schnell et al., 2018). Earlier research (Kolck et al., 2026, 2023b, 2023a; Witte et al., 2023) concentrated on the gas phase hetero-agglomeration process itself using exemplary materials. This work directly addresses the hetero-agglomeration of ASSB materials with the objective of contributing to the development of a production method for all-solid-state cathode materials consisting of lithium iron phosphate ($\mathrm{LiFePO_4}$, LFP) as active material, lithium indium chloride ($\mathrm{Li_3InCl_6}$, LIC) as solid electrolyte and carbon black (CB) as conductive additive. LFP and LIC are present in the form of particles and CB is present in the form of stable aggregates. The size and morphology of these aggregates will be discussed in Section 2.2.1. A description of the considered solid electrolyte in the context of potential all-solid-state battery materials is provided in (Frankenberg et al., 2024).

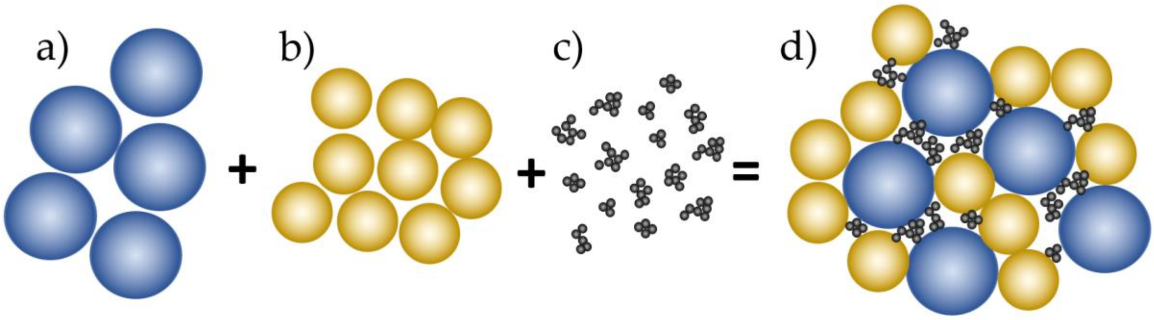

Fig. 1 a) Cathode active material, b) solid electrolyte and c) carbon black aggregates, forming a solid-state battery cathode hetero-agglomerate d).

Hetero-agglomerates can form through three distinct processes: first, in the liquid phase (Gunlazuardi et al., 2021; Q. Li et al., 2019; Liu et al., 2022); second, through mechanical mixing (Poux et al., 1991); or third, in the gas phase (Buchheiser et al., 2023; Gerken et al., 2023; Witte et al., 2023). The advantages and limitations of these methods are discussed in (Kolck et al., 2023a). Recently, a jet-based direct mixing gas-phase hetero-agglomeration process was introduced and analysed both numerically (Kolck et al., 2023a) and experimentally (Witte et al., 2025, 2023). This process involves deagglomerating particles to the primary particle level using a rotating brush disperser, followed by turbulent mixing of two crossing particle-laden jets. In the mixing zone, particles of different materials contact and form hetero-agglomerates. As the results of (Kolck et al., 2023a) indicated a deficiency in particle concentration and residence time, the original process was reformulated in (Kolck et al., 2026) to eliminate the need for a secondary carrier gas (a third stream used to remove agglomerates), thereby increasing the particle-to-gas volume ratio.

The turbulent pipe flow of this process, which plays a role in facilitating further mixing and agglomeration, was recently the subject of numerical investigations in (Kolck et al., 2026). In that study, a Lagrangian particle tracking and agglomeration approach (Sommerfeld and Stübing, 2017) was employed to model the particle motion as well as mixing and agglomeration of micrometre-sized particles in turbulent pipe flows. In this context, the fluid field, comprising the mean flow velocities and the root-mean-square (RMS) values of the velocity fluctuations, was provided by suitable curve-fit functions derived from direct numerical simulation (DNS) data. The RMS velocities were employed for the modelling of turbulent dispersion via an improved discrete random walk model (IDRW) (Mofakham and Ahmadi, 2020), while the agglomeration was modelled using a Lagrangian agglomerate structure model proposed by (Sommerfeld and Stübing, 2017). The findings indicated that the selection of pipe diameter and mixing configuration exerts a significant influence on the size and composition of hetero-agglomerates. Specifically, the ratio of hetero- to homo-contacts was found to be dependent on the pipe diameter-dependent turbulent intensity, provided that the surface energies of the hetero-materials in question exhibit significant disparities. Moreover, the interplay between deposition and agglomeration results in a local maximum of hetero-contact formation.

The methodology employed in (Kolck et al., 2026) is particularly well-suited to the context of ASSB cathode materials for which it was not yet directly considered. This is due to the fact that the methodology, which is comparatively less computationally intensive than time-resolved modelling of collisions of individual particles in discrete element method (DEM) simulations, enables a great number of very small particles to be handled. Conversely, the approach is nevertheless capable of representing the agglomerate structure, thereby offering an effective compromise between computational efficiency and modelling accuracy. The simulation approach presented in (Kolck et al., 2026) is used for modelling the agglomeration, dispersion and deposition of ASSB cathode material particles in turbulent pipe flows as part of the proposed gas phase hetero-agglomeration process. In this work, an appropriate pipe diameter is selected based on the interplay of deposition and agglomeration. The parallel and sequential mixing and agglomeration of CAM, SE particles and CB aggregates in different combinations are then analysed to identify the resulting differences in structure, composition, size and amount of hetero-agglomerates formed.

The article is structured as follows. In Section 2, the methods utilized are outlined. This encompasses the numerical methodologies employed in the simulations, in addition to a detailed exposition of the characterization of the initial materials. The latter encompasses the reconstruction of the initial CB aggregates, the measurement of the particle size distributions, and the determination of the surface energies of all materials. This is followed by a description of the simulation setup, including the simulation conditions and workflow for parameter variation and optimization (Section 3). In Section 4, the results of all simulation sets in this workflow are discussed individually. Conclusions are finally drawn in Section 5.

2 Methods

The methods described in this section are divided into two main parts. Section 2.1 presents simulation methods, including modeling particle and agglomerate motion, as well as agglomeration processes in turbulent flows. Section 2.2 describes the experimental and numerical methods used to characterize the starting materials, such as carbon black aggregate reconstruction, particle size distribution measurements, and surface energy determination.

2.1 Modelling agglomeration in turbulent pipe flows

2.1.1 Particle motion

The methodology employed in this study for modelling dispersion and agglomeration in turbulent pipe flows is described in detail in previous work (Kolck et al., 2026). However, a concise summary is provided here for the reader's convenience. In addition, certain modifications have been made to the original model, and these are detailed below. Following the Lagrangian particle tracking method, the motion of a spherical particle or agglomerate is described by Newton's equation of motion, which is integrated over time and given as

$$m_{\mathrm{p}} \frac{d^2 \vec{x}_{\mathrm{p}}}{dt^2} = \vec{F}_{\mathrm{p}}^{\mathrm{D}} + \vec{F}_{\mathrm{p}}^{\mathrm{L}} + \vec{F}_{\mathrm{p}}^{\mathrm{Br}} + m_{\mathrm{p}} \vec{g}, \tag{1}$$

where a p in the in the index of a variable is, from here on, used to emphasize that the variable is a descriptor of a particle or agglomerate. In Eq. (1) the sum of all three-dimensional forces acting on a particle can be expressed as the product of the particle mass m_{p} and the particle/agglomerate acceleration $d^2\vec{x}_\mathrm{p}/dt^2$, where $\vec{x}_\mathrm{p}$ is the three-dimensional particle/agglomerate location and t is the time. The individual forces that are considered here are to be found on the right-hand side of Eq. (1). The forces $\vec{F}_\mathrm{p}^\mathrm{D}$, $\vec{F}_\mathrm{p}^\mathrm{L}$ and $\vec{F}_\mathrm{p}^\mathrm{Br}$ are, the fluid drag force, the lift force and the Brownian force, respectively. The gravitational force is represented by $m_\mathrm{p}\vec{g}$, where $\vec{g}$ is the three-dimensional gravitational acceleration vector.

It is important to note that the modelling framework utilizes the so-called parcel concept, in which each computational particle (parcel) represents a defined number $N_\mathrm{p}^\mathrm{P} \epsilon \mathbb{N}$ of particles with the same properties (Kolck et al., 2026; Sommerfeld and Stübing, 2017). In the present work, this concept is also followed for the initial CB aggregates (details given later).

The drag force $\vec{F}_\mathrm{p}^\mathrm{D}$ depends on the particle/agglomerate Reynolds number and on the relative velocity between the particle/agglomerate and the fluid. The Cunningham slip correction factor is also considered in the calculation of this force, and the drag coefficient is given by the expression of (Schiller and Naumann, 1933). The fluid velocities that are needed to calculate the drag force are composed of a mean flow velocity component and a turbulent fluctuation velocity component. Both the mean flow velocity and the root-mean-square (RMS) values of the velocity fluctuations are determined through curve-fits of DNS data from (El Khoury et al., 2013), as provided in (Kolck et al., 2026). The resulting continuous and wall-distance-dependent functions of the anisotropic RMS velocity fluctuations are utilized to model the actual time-dependent fluctuation velocities acting on a particle. This is achieved through the implementation of an improved discrete random walk model, as proposed by (Mofakham and Ahmadi, 2020), which extends the conventional discrete random walk model (Gosman and Ioannides, 1983) by incorporating a drift velocity correction term. This modification serves to prevent a spurious accumulation of very small particles in regions of low turbulence (see (Mofakham and Ahmadi, 2020) for further details). The model employs a stochastic representation of turbulent eddies in a real flow, which act on the particles. Realizations of Gaussian random vectors are drawn to model the fluctuation velocities, which scale the RMS velocity fluctuations in each specific direction. The realizations are drawn after a specified time interval to describe how long a particle is affected by the same eddy. The time interval between generating new random vectors for a single particle depends on the turbulent length scale and the time it takes the particle to cross an eddy.

The lift force $\vec{F}_{\mathrm{p}}^{\mathrm{L}}$ acting normal to the wall, which is induced by the strong flow shear in the turbulent boundary layer, is modelled using the expression proposed by (Mclaughlin, 1993) and a curve-fit given by (Mei, 1992). This approach offers a relaxation of the restrictions of the original expression given by (Saffman, 1968, 1965). The Brownian force $\vec{F}_{\mathrm{p}}^{\mathrm{Br}}$ is only relevant for fluid-tracer-like particles and is represented by a Gaussian white noise random process (Li and Ahmadi, 1993), whereby a Gaussian random number vector is generated at each time step in order to model the magnitude scaling and direction of a particle and temperature-dependent force.

2.1.2 Agglomeration

The previously discussed discrete random walk model effectively captures the stochastic particle trajectories in turbulent pipe flows. However, it is unable to account for the correlations that exist between these trajectories. As a result, it is unable to predict the actual relative positions and velocities of the particles, which are usually relevant for modelling agglomeration. In order to address this issue, a stochastic inter-particle collision model (Sommerfeld, 2001) within the framework of the Lagrangian agglomerate structure model introduced by (Sommerfeld and Stübing, 2017) is employed.

The initial step in the inter-particle collision model is to ascertain the relative velocity between a given particle and another, fictitious particle, as well as the probability of their collision. The frequency of particle collisions and the underlying mean particle relative velocity are contingent on the ratio of the particle relaxation time τ_{p} (Kolck et al., 2026) to the turbulent time scales. The ratio of the particle relaxation time τ_{p} to the Lagrangian integral time T_{L} is expressed by the large-scale Stokes number

$$\mathrm{St}_{\mathrm{L}} = \frac{\tau_{\mathrm{p}}}{T_{\mathrm{L}}}. \qquad (2)$$

As discussed below, for certain collision mechanisms the particle relaxation time τ_p is related to the Kolmogorov time scale T_k by:

$$\mathrm{St}_\mathrm{k} = \tau_\mathrm{p}/T_\mathrm{k}. \tag{3}$$

The Kolmogorov time scale (Kolmogorov, 1991), defined as the characteristic time scale of the smallest turbulent eddies, is given by

$$T_\mathrm{k} = \sqrt{\frac{\nu_\mathrm{f}}{\varepsilon}}, \tag{4}$$

where ν_f is the kinematic viscosity of the fluid and ε is the turbulent energy dissipation rate. (Zaripov et al., 2019) measured the non-dimensional turbulent energy dissipation rate ε^+ over the non-dimensional wall distance y^+ and the results have been curve-fitted in order to estimate the dissipation profile, which is given by

$$\varepsilon^+ = 0.2019\,\exp(-0.043\,y^+) + 0.0225. \tag{5}$$

This approach is essentially congruent with the preceding procedure for the determination of the RMS velocities. The curve-fit in comparison to the experimental data from (Zaripov et al., 2019) is illustrated in Fig. A1 in the Appendix. It should be noted that the symbol "+" is used to indicate non-dimensional flow variables. For a detailed description of the non-dimensional variables and their conversion to physical variables, please refer to (Kolck et al., 2026). The collision rate of particles in turbulent flows is governed by several effects throughout a wide range of scales of fluid motion (Wang et al., 2000). The highest relative particle velocities are observed for particle relaxation times that are similar to the Lagrangian integral time scale T_L ($\mathrm{St}_\mathrm{L} = \frac{\tau_\mathrm{p}}{T_\mathrm{L}} = O(1)$) (Williams and Crane, 1983). These phenomena are induced by the large-scale energetic eddies and result in elevated collision rates (turbulent transport effect) (Zhou et al., 2001). For particles exhibiting a relaxation time that is comparable to the Kolmogorov time scale ($\mathrm{St}_\mathrm{k} \approx 1$), the accumulation effect is most pronounced (Zhou et al., 2001). This effect is characterized by the local non-uniform particle distribution and the preferential concentration of particles at the interface of dissipation-scale turbulent eddies, which leads to an increased collision probability. The relative velocities of small Stokes numbers are predominantly induced by differences in the particle relaxation time (acceleration induced) or by turbulent shear (Williams and Crane, 1983).

In the model outlined in (Kolck et al., 2026), the inter-particle collision probability for a real particle colliding with another, fictitious particle, was determined in accordance with the findings of Williams and Crane (Williams and Crane, 1983), who provided a formulation for the collision kernel and the collision velocities due to the collision mechanisms of turbulent shear and particle acceleration. However, it has been demonstrated that the inherent expression for the energy spectrum is not applicable in the viscous subrange of turbulence (Kruis and Kusters, 1997). This restriction is violated in the case of the small CB aggregates (see Section 2.2.1) considered here, since their relaxation times can be smaller than the Kolmogorov time scales ($\mathrm{St}_\mathrm{k} < 1$). (Kruis and Kusters, 1997) reformulated the model, thereby removing the restriction that Stokes numbers must be greater than one. In their study of bidisperse particle collisions, (Zhou et al., 2001) employed this reformulation and calibrated the parameters to their DNS results, thereby deriving a semi-empirical model that encompasses shear- and acceleration-induced collision mechanisms in turbulence extending into the viscous subrange. Moreover, the impact of the local particle preferential concentration on the collision kernel is considered within the framework of this theory.

Recall that the work presented here employs the parcel framework, in which particles sharing identical composition and diameter d_i are assembled into a single parcel $i \in I$, where I denotes the set of all possible parcels. Furthermore, each parcel is assigned an associated multiplicity N_i^P representing the number of particles it comprises.

Generally, the collision probability $P_{ij}\colon (0,\infty) \to (0,\infty)$ of a particle within a parcel $i \in I$ with another, fictitious particle of parcel $j \in I$, and radial relative velocity $v_{ij,\mathrm{r}}$ is given by

$$P_{ij}(v_{ij,\mathrm{r}}) \; = \Gamma_{ij}(v_{ij,\mathrm{r}})\, n_\mathrm{p}\, N_i^\mathrm{P}\, \Delta t, \tag{6}$$

where $n_\mathrm{p} = \sum_{i \in I} N_i^\mathrm{P}$ is the particle number density within the local computational cell of size $[\frac{1}{m^3}]$. The simulation time step is denoted by Δt, which in this work is set to $\Delta t = 1.09 \times 10^{-7}\ s$, and $\Gamma_{ij}\colon \mathbb{R} \to (0,\infty)$ $[\frac{m^3}{s}]$ is the collision kernel (Wang et al., 2000). For two particles of the parcels $i,j \in I$ with relative radial velocity $v_{ij,\mathrm{r}}$, the collision kernel is given by

$$\Gamma_{ij}(v_{ij,\mathrm{r}}) = \frac{\pi}{2}\left(d_i + d_j\right)^2 |v_{ij,\mathrm{r}}|\, g_{ij}\, \beta_{ij} = \Gamma_{ij,0}(v_{ij,\mathrm{r}})\, g_{ij}\, \beta_{ij}, \tag{7}$$

where $\Gamma_{ij,0}\colon \mathbb{R} \to (0,\infty)$ $[\frac{m^3}{s}]$ is here referred to as the fundamental collision kernel, the real number $1 \geq \beta_{ij} \geq 0$ is the collision efficiency and g_{ij} is the radial distribution function (RDF), describing the probability density of finding a contacting particle pair with a collision radius of $\frac{1}{2}\left(d_i + d_j\right)$ in the actual spatial dispersion relative to the value expected for a uniformly distributed dispersion (Wang et al., 2000; Zhou et al., 2001).

In the present modelling approach, the particle velocities are not correlated to each other and information about the actual relative velocities are missing. Therefore, the approach described by (Zhou et al., 2001) is utilized. More precisely, it is assumed that the relative velocity between two particles of the parcels $i,j \in I$ can be described by a Gaussian distributed random variable with zero mean and standard deviation σ_{ij}^{v} , given by

$$\sigma_{ij}^{\mathrm{v}} = \sqrt{\left\langle {v_{ij,\mathrm{r}}^{\mathrm{a}}}^2 \right\rangle + \left\langle {v_{ij,\mathrm{r}}^{\mathrm{s}}}^2 \right\rangle}, \tag{8}$$

where $\left\langle {v_{ij,\mathrm{r}}^{\mathrm{a}}}^2 \right\rangle$ is the acceleration induced mean square radial relative velocity and $\left\langle {v_{ij,\mathrm{r}}^{\mathrm{s}}}^2 \right\rangle$ is the turbulent shear induced mean square radial relative velocity (Zhou et al., 2001), given by

$$\sqrt{\left\langle {v_{ij,\mathrm{r}}^{\mathrm{s}}}^2 \right\rangle} = \sqrt{\frac{\varepsilon}{15\,\nu_{\mathrm{f}}}}\,\frac{1}{2}(d_1 + d_2). \tag{9}$$

The acceleration induced relative radial velocity depends on the large-scale Stokes number St_{L} and the local fluid RMS velocity u'_{f}. It is given by

$$\sqrt{\left\langle {v_{ij,\mathrm{r}}^{\mathrm{a}}}^2 \right\rangle} = \sqrt{(1 + 0.6\exp(-(\alpha - 1)^{1.5}))\left\langle {v_{ij}^{\mathrm{a}}}^2 \right\rangle}, \tag{10}$$

where the square of the relative RMS velocity is calculated by

$$\left\langle {v_{ij}^{\mathrm{a}}}^2 \right\rangle = u_{\mathrm{f}}^{\prime 2}\, \frac{\gamma}{\gamma-1}\left((\theta_i+\theta_j)^2 - \frac{4\,\theta_i\theta_j}{(\theta_i+\theta_j)}\sqrt{\frac{1+\theta_i+\theta_j}{(1+\theta_i)(1+\theta_j)}}\right)\left(\frac{1}{(1+\theta_i)(1+\theta_j)} - \frac{1}{(1+\gamma\theta_i)(1+\gamma\theta_j)}\right), \tag{11}$$

where $\theta_k = 2.5\,\mathrm{St}_{\mathrm{L},k}\ , k \in I$ is a scaling of the Stokes number $\mathrm{St}_{\mathrm{L},k}$ and $\gamma = \alpha \times 0.183\, u_{\mathrm{f}}'^2 / \sqrt{\varepsilon \nu_{\mathrm{f}}}$ is an empirical modification function, where

$$\alpha = \max(\theta_i/\theta_j\,, \theta_j/\theta_i) \tag{12}$$

is the Stokes number ratio (Wang et al., 2000; Zhou et al., 2001).

Adopting this approach permits the assignment of a random relative velocity between a real and a fictitious particle to each probable collision event and the fundamental collision kernel $\Gamma_{ij,0}$ can be calculated.

As previously mentioned, the actual collision kernel Γ_{ij} in Eq. (7) can be affected by further phenomena. The collision efficiency β_{ij} is a measure of the decrease in collision frequency due to the hydrodynamic interaction of the particles. Particularly when small CB aggregates (see Section 2.2) collide with a significantly larger particle designated as the "collector", they may follow the streamlines around the collector without coming into direct contact with it. According to (Slinn, 1977), the collision efficiency can be expressed as the sum of different mechanisms contributing to impingements of a small particle/aggregate onto a larger one. The collision efficiency β_{ij} is given by

$$\beta_{ij} = \beta_{ij}^{\mathrm{imp}} + \beta_{ij}^{\mathrm{int}} + \beta_{ij}^{\mathrm{Br}} \tag{13}$$

and is composed of three contributions: the collision efficiency due to inertial impaction $1 \geq \beta_{ij}^{\mathrm{imp}} \geq 0$, due to interception $1 \geq \beta_{ij}^{\mathrm{int}} \geq 0$ and due to Brownian motion $1 \geq \beta_{ij}^{\mathrm{Br}} \geq 0$. The subsequent discussion will address each of these contributions in turn. Inertial impaction describes the effect of particles being unable to follow the streamlines around the larger particle due to its inertia. This effect, which is dominant for larger particles, has been considered in previous work (Kolck et al., 2026) by employing the approach of (Schuch and Löffler, 1978). Here, the inertial impaction collision efficiency is determined by the expression provided by (Slinn, 1977) and is given by

$$\beta_{ij}^{\mathrm{imp}} = \left(\frac{\mathrm{St}_{\mathrm{rel}} - \mathrm{St}_{\mathrm{rel}}^{*}}{\mathrm{St}_{\mathrm{rel}} - \mathrm{St}_{\mathrm{rel}}^{*} + 2/3}\right)^{3/2}, \tag{14}$$

where $\mathrm{St}_{\mathrm{rel}}^{*}$ is the critical relative Stokes number, at which inertial impaction ceases to occur. The relative Stokes number, $\mathrm{St}_{\mathrm{rel}}$, is a measure of the ability of the impinging particle with a relative velocity v_{ij} to follow the streamlines around the collector (indexed C) with radius r_{C}. It is defined as the ratio of the particle relaxation time to the passing time and is given by

$$\mathrm{St}_{\mathrm{rel}} = \frac{\tau_{\mathrm{p}}\, v_{ij}}{r_{\mathrm{C}}}. \tag{15}$$

According to (Slinn, 1977), the critical relative Stokes number $\mathrm{St}_{\mathrm{rel}}^{*}$ is expressed as

$$\mathrm{St}_{\mathrm{rel}}^{*} = \frac{1.2 + 1/12\,\ln(1+\mathrm{Re}_{\mathrm{C}})}{1+\ln(1+\mathrm{Re}_{\mathrm{C}})}, \tag{16}$$

where the collector Reynolds number Re_{C} is defined as

$$\mathrm{Re}_{\mathrm{C}} = \frac{R_{\mathrm{C}}\, v_{ij}}{\nu_{\mathrm{f}}}. \tag{17}$$

The interception collision efficiency $\beta_{ij}^{\mathrm{int}}$ is a measure that assesses the effect of particles that follow the streamlines around the collector without inertia effects. In such instances, collision is possible if the closest distance of the streamline to the collector surface is smaller than the particle radius r_{p}. The interception collision efficiency $\beta_{ij}^{\mathrm{int}}$ is contingent on the collector Reynolds number, as well as the size ratio of the small particle with a radius r_{p} to the collector with radius r_{C} and is given by

$$\beta_{ij}^{\mathrm{int}} = 4\left(\frac{r_{\mathrm{p}}}{r_{\mathrm{C}}}\right)^{2}\left(1 + 2\sqrt{\mathrm{Re}_{\mathrm{C}}}\right). \tag{18}$$

It is important to note that the formulation in Eq. (18) has been derived in (Slinn, 1977) for the limit of infinite viscosity ratios, i.e., viscosity of the fluid to viscosity of the collector, thereby rendering the model applicable to the case of solid collectors considered here.

In contrast to previous work (Kolck et al., 2026), which solely accounted for the inertial collision efficiency by the model of (Schuch and Löffler, 1978), it is imperative here to consider the collision efficiency associated with Brownian motion β_{ij}^{Br}. The present investigation concerns small carbon black aggregates, which interact with air molecules through random collisions. This random motion has been shown to increase the collision efficiency of small aggregates/particles passing the collector. Following (Slinn, 1977), the collision efficiency due to Brownian motion β_{ij}^{Br} is given by

$$\beta_{ij}^{\mathrm{Br}} = \frac{4}{\mathrm{Re_C\,Sc}}\left(1 + 0.4\sqrt{\mathrm{Re_C}}\,\mathrm{Sc}^{1/3} + 0.16\sqrt{\mathrm{Re_C\,Sc}}\right), \tag{19}$$

where the Schmidt number Sc of the smaller, approaching particle/aggregate is

$$\mathrm{Sc} = \frac{\nu_\mathrm{f}\,6\pi\mu_\mathrm{f}r_\mathrm{p}}{(k_\mathrm{B}TC_\mathrm{sc})}, \tag{20}$$

where $k_\mathrm{B} = 1.38 \times 10^{-23}\ \mathrm{J/K}$ is the Boltzmann constant, μ_f is the dynamic viscosity of the fluid, C_sc is the Cunningham slip correction factor (Cunningham, 1910) and $T\ [K]$ is the absolute temperature, which is set to $293.15\ \mathrm{K}$ in all simulations.

The collision kernel in Eq. (7) is further affected by the accumulation effect, defined as the local preferential concentration between turbulent eddies, which is quantified by the RDF g_{ij}. A formulation for g_{ij} is provided in (Zhou et al., 2001), which is contingent on the Kolmogorov Stokes number $\mathrm{St_k}$ and is also applicable to collisions of bidisperse particles. The RDF g_{ij} of an actual turbulent bidisperse dispersion is expressed in terms of the RDFs g_{ii} and g_{jj} of the individual fractions and is given by

$$g_{ij} = 1 + \vartheta_{ij}\sqrt{(g_{ii}-1)(g_{jj}-1)}. \tag{21}$$

The two preferential concentration functions are correlated by a concentration correlation coefficient ϑ_{ij}, which can be expressed as a function of the Stokes number ratio, α (see Eq. (12)). The correlation coefficient has been fitted by (Zhou et al., 2001) and writes

$$\vartheta_{ij}(\alpha) = 2.6\exp(-\alpha) + 0.1025\ \exp(-0.0206\,\alpha) \times (1 + \tanh(\alpha - 3))\,. \tag{22}$$

The RDF at contact g_{ii} and g_{jj} for monodisperse particles can be described as a function of the Taylor- microscale Reynolds number of the flow, $\mathrm{Re}_\lambda = u_\mathrm{f}'^2\sqrt{15/(\nu_\mathrm{f}\,\varepsilon)}$, and $\mathrm{St_k}$. According to (Wang et al., 2000), the RDF for a particle $i \in I$ is given by

$$g_{ii} = 1 + y_0[1 - z_0^2] + \mathrm{Re}_\lambda\,z_0^2\{y_1[1 - z_1] + y_2 z_1 + y_3\,z_2\}\,, \tag{23}$$

where the curve-fitted functions y_0, y_1, y_2 and y_3 were constructed for different regions of the Kolmogorov Stokes number $\mathrm{St}_{\mathrm{k},i}$ of the particle i, and the functions z_0, z_1 and z_2 are smooth transition functions:

$$
\begin{aligned}
&y_0(\mathrm{St}_{\mathrm{k},i}) = 18\,\mathrm{St}_{\mathrm{k},i}^2, \\
&y_1(\mathrm{St}_{\mathrm{k},i}) = 0.36\,\mathrm{St}_{\mathrm{k},i}^{2.5}\exp\left(-\mathrm{St}_{\mathrm{k},i}^{2.5}\right), \qquad && y_2(\mathrm{St}_{\mathrm{k},i}) = 0.24\exp(-0.5\,\mathrm{St}_{\mathrm{k},i}) \\
&y_3(\mathrm{St}_{\mathrm{k},i}) = 0.013\exp\left(-0.07\,\mathrm{St}_{\mathrm{k},i}\right), && z_0(\mathrm{St}_{\mathrm{k},i}) = \frac{1}{2}\left(1+\tanh\left(\frac{\mathrm{St}_{\mathrm{k},i}-0.5}{0.25}\right)\right), \\
&z_1(\mathrm{St}_{\mathrm{k},i}) = \frac{1}{2}\left(1+\tanh\left(\frac{\mathrm{St}_{\mathrm{k},i}-1.25}{0.1}\right)\right), && z_2(\mathrm{St}_{\mathrm{k},i}) = \frac{1}{2}\left(1+\tanh\left(\frac{\mathrm{St}_{\mathrm{k},i}-6.5}{2.5}\right)\right).
\end{aligned}
\tag{24}
$$

As demonstrated in Eq. (23), it is evident that the accumulation effect is significantly impacted by the Taylor microscale Reynolds number. For flows with very large Re_λ and particles with $\mathrm{St}_\mathrm{k} \approx 1$, the collision probability may be increased by several orders of magnitude when compared to scenarios where the accumulation effect is disregarded.

For each pair of a real particle and a fictitious particle randomly selected out of all particles in a cell (see (Sommerfeld, 2001)), the collision velocity is determined by calculating its standard deviation according to Eq. (8). For a given simulation time step and cell particle concentration, the collision probability can then be calculated by Eq. (6) and (7), which account for the accumulation effect and the collision efficiency. In order to ascertain whether a collision occurs, a random number is drawn from a uniform distribution in the interval [0, 1] and is compared to the respective probability. If the collision probability exceeds the drawn random number, a collision is regarded as having occurred. In the case of an impingement, the collision velocity is compared to a critical collision velocity in order to ascertain whether the particles can be assumed to be agglomerated or not (for details on the procedure see (Kolck et al., 2026)). The critical velocity is computed initially for each simulation, for every particle type combination, through 1D-DEM simulations of straight collisions in the framework of a Newton scheme.

In the case of a particle colliding with an agglomerate or CB aggregate, this procedure is conducted for the impinging particle and the inner-agglomerate particle that initially has contact with the other (Sommerfeld and Stübing, 2017). In the case of two agglomerates colliding with each other, the effective collision energy is compared with the energy needed for the loss of one particle, as well as for the complete destruction of the agglomerates (Kolck et al., 2026). These calculations are performed in accordance with the expressions provided by (Dominik and Tielens, 1997). Within the present modelling framework, CB aggregates are treated as mechanically rigid, sintered particle-structures (further details on the morphology can be found in Section 2.2.1). Due to their considerably smaller mass and length scale compared to LFP and LIC particles, CB-CB contacts are not considered to govern fragmentation at the agglomerate scale. Therefore, they are excluded from the calculation of the collision outcome and CB particles are considered not to be detachable. In the specific case of two colliding LFP or LIC particles that have already undergone agglomeration with CB, the collision outcome is calculated based on the critical velocity of these particles. This approach is reasonable, given that the masses of the carbon black aggregates are two to three orders of magnitude smaller than those of LFP and LIC.

2.2 Characterization of starting materials

This paper investigates a submicron particle system as a cathode material for use in ASSBs. LFP serves as the active electrode material, which is responsible for storing and releasing lithium ions. LFP is suitable for several reasons, in particular due to its high thermal and electrochemical stability, long lifetime, comparatively high cycling stability, good environmental compatibility, and low material costs (Wang et al., 2012). The active material used in this work is a submicron LFP with a primary particle size of $530\,\mathrm{nm}$ (E-P2, Epsilon Cam GmbH, Germany).

CB (C45, Imerys, France) is added to the composite to increase its electronic conductivity. CB forms a percolating network of electronic pathways within the cathode, thereby compensating for the low electronic conductivity of LFP. The CB used is present in the form of stable aggregates which promotes a high specific surface area and supports the formation of an efficient conductive network structure (Spahr et al., 2011).

The solid electrolyte LIC is used as the ionically conductive component. LIC is characterized by high lithium ion conductivity of up to $2.04\ \mathrm{mS/cm}$ at 25 °C, enabling the formation of stable and efficient ionic transport paths within the cathode composite (X. Li et al., 2019). In addition, LIC exhibits increased chemical and electrochemical stability against moisture and common cathode active materials. The LIC used is self-synthesized and described in (Frankenberg et al., 2024).

2.2.1 Carbon black aggregate reconstruction

Real carbon black (C45) exists in the form of stable primary aggregates with sizes of $100 - 400\ \mathrm{n}m$ (Weber and Friedlander, 1997), rather than single primary particles (see Fig. 2 a)). The primary particles within these aggregates are connected by rigid bonds. Assuming the CB to be in the form of single primary particles in the simulations would lead to spurious motion in the fluid, agglomeration, and agglomerate structure. Therefore, the present simulation approach requires realistic, three-dimensional (3D) virtual aggregate geometries as a starting material. This ensures that the virtual primary CB aggregates have realistic Stokes numbers and mimic the positions of the primary carbon black particles within formed hetero-agglomerates.

Due to the small length scales of the aggregates, a direct reconstruction from 3D experimental techniques such as nano-computed tomography is not feasible. This is mainly caused by excessive acquisition times, high costs, and substantial sample preparation effort. To overcome these limitations, 3D aggregates are not derived directly from volumetric measurements. Instead, realizations of a stochastic 3D geometry model are employed as simulation input. By stereologically calibrating this 3D stochastic model using two-dimensional (2D) image data, computational feasibility is ensured while preserving statistically realistic microstructural features derived from experimental data (Fuchs et al., 2025a, 2025b).

2.2.1.1 Stochastic aggregate model

The aggregate model considered in this work is based on the concept of cluster-cluster aggregation. In this framework, aggregates are formed through successive aggregation of smaller particle clusters (Sorensen, 2011). More precisely, the stochastic geometry model is based on the approach described in (Fuchs et al., 2024). The model allows for the generation of aggregates with desired size and fractal dimension (Filippov et al., 2000; Mandelbrot, 1982), thereby controlling both the overall extent and the morphology of the aggregates.

In (Fuchs et al., 2024), the aggregation process consists of two stages. First, small clusters are generated by particle-cluster aggregation. Starting from a single particle, additional particles are iteratively added to the cluster. For each new particle, a spatial position is sampled uniformly from the set of admissible positions. This admissible set is defined by three constraints: the resulting aggregate must comprise contacting particles which must not overlap each other, and the fractal dimension of the cluster must match a desired one. Since the set of admissible particle positions cannot be described analytically, in (Fuchs et al., 2024), uniform sampling from this set is realized using acceptance-rejection sampling (Ripley, 1987). Candidate positions satisfying the fractal dimension constraint are generated first and subsequently tested for the other constraints. Positions violating these conditions are rejected and resampled.

In the second stage, larger aggregates are formed by aggregating the previously generated clusters using the same acceptance-rejection sampling method. In (Fuchs et al., 2024), aggregates consisting of approximately 50 particles were considered. However, in the present work, aggregates containing up to 150 particles are desired. For such a number of particles, the computational cost of pure acceptance rejection sampling becomes prohibitive. Therefore, the model is slightly modified to ensure computational feasibility. Specifically, instead of rejecting infeasible positions outright, a forced bias algorithm (Mościński et al., 1989) is applied to adapt sampled positions iteratively. If a sampled position leads to particle overlap, repulsive forces proportional to the overlap depth and directed along the separation vector are introduced. If the position would result in a disconnected aggregate, an attractive force proportional to the distance to the nearest particle in the aggregate is applied. In each iteration, the mean force resulting from all active constraints is computed and the candidate position is updated accordingly. The forced bias algorithm terminates once no forces act on the position, yielding a valid placement that satisfies connectivity and non-overlap. If convergence is not achieved after 1000 iterations, the procedure is terminated and a new initial position is drawn. If the forced bias algorithm terminates successfully, it guarantees connectivity and non-overlap but may violate the fractal dimension constraint. Since the displacement relative to the initially sampled position is small and decreases in relative importance with increasing aggregate size, this deviation is considered negligible for the aggregates studied here.

In the SEM image data (see Fig. 2 a)) it is evident that the considered aggregates consist of strongly sintered particles rather than particles that merely touch at isolated contact points. To account for this effect, a virtual sintering step is applied to aggregates generated by the procedure described above. First, all primary particles are uniformly dilated by a prescribed dilation radius (Schneider, 2013). This dilation introduces controlled overlaps between neighboring particles. Subsequently, a morphological closing operation is applied to the entire aggregate. This operation compensates for the overlaps introduced by the dilation by adding the volume of these overlaps at particle junctions, thereby forming solid neck regions between adjacent particles, similar to those observable in sintered aggregates (compare Fig. 2 a) and Fig. 3 a) and b)). In total, the stochastic aggregation model contains five tunable parameters: the initial cluster size used in particle cluster aggregation, the total number of primary particles per aggregate, the target fractal dimension, the particle radius and the dilation radius.

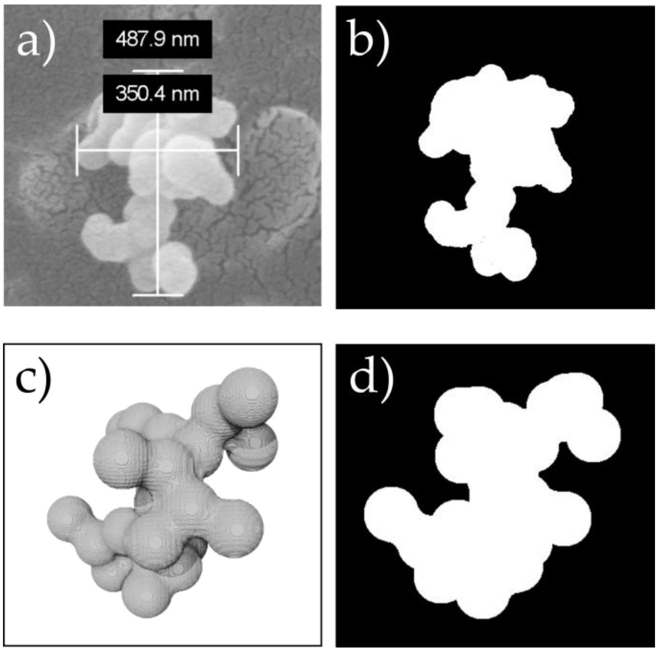

Fig. 2 Projection data of an aggregate: a) Measured SEM image of a C45 CB aggregate, b) segmentation of the aggregate from the background corresponding to a), c) virtual aggregate and d) virtual projection corresponding to the aggregate shown in c).

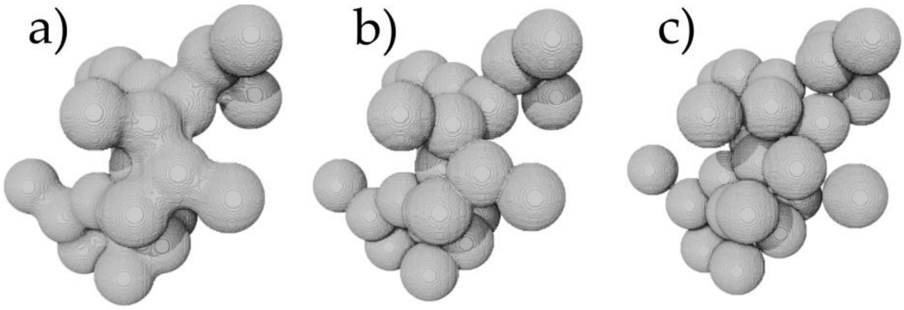

Fig. 3 Virtual 3D aggregate: a) Virtual aggregate consisting of 28 particles, b) virtual aggregate after reversing morphological closing and c) result of applying a forced-bias algorithm to resolve particle overlaps. This is used as input for the simulation and shows high similarity to the aggregates shown in a) and b).

2.2.1.2 Aggregate model calibration

The calibration of the model parameters is based on 2D scanning electron microscopy image data. An exemplary SEM image is shown in Fig. 2 a). Individual primary particles are manually labeled and segmented to estimate the primary particle size distribution. Based on this analysis, a monodisperse distribution with primary particle diameter of 54 nm is determined as a model parameter. In addition, the effective overlap of primary particles caused by sintering is estimated manually from the SEM images. An average overlap of 20% of the particle radius is estimated. The initial cluster size of the aggregation model is set heuristically to be uniformly distributed between 5 and 10. The remaining parameters, namely the number of primary particles per aggregate and the fractal dimension, are estimated using the 2D dimensional box counting method (Stanley and Ostrowsky, 1985). In this approach, a binary image of an aggregate is recursively subdivided into square boxes of decreasing size. For each box width, the number of boxes intersecting the aggregate is counted. The total number of intersecting boxes (the ordinate in Fig. 4 a) and b)) provides a measure of the necessary primary particle number, while the slope of the logarithm of the number of intersecting boxes versus the logarithm of the box size (see Fig. 4) yields an estimate of the fractal dimension. See (Stanley and Ostrowsky, 1985) for further details.

Prior to box counting, the measured SEM images are binarized using a non-local means filter (Buades et al., 2005; Russ, 2006) followed by Otsu thresholding (Otsu, 1979). One result of this procedure is shown in Fig. 2 b). For each realization of the stochastic aggregate model, a virtual 2D binarized projection is computed too. Box counting is then applied to both experimental and virtual images. This procedure was carried out for nine virtual aggregates, yielding fractal dimensions ranging from 1.5 to 2.7, and desired aggregate particle numbers ranging from 25 to 138, in order to obtain the closest match in box counting statistics. The virtual aggregates feature diameters ranging from 201 to 411 nm, which directly result from the fractal dimension and particle number. As these nine reconstructed aggregates cover a certain range of fractal dimensions and aggregate sizes, they are expected to represent the real occurrence of the CB to a certain extent rather than using single CB primary particles as the initial material, as is done in conventional simulation approaches (Sangrós Giménez et al., 2020). The box counting results for the measured aggregates are shown in Fig. 4 a), while the corresponding results for virtual aggregates are shown in Fig. 4 b), and the two sets of results match well.

The procedure described above is designed to reproduce the measured aggregates as closely as possible in a statistical sense. However, the subsequent simulations require aggregates consisting of strictly non-overlapping spheres. Therefore, the morphological closing implied by sintering is reversed and a second application of the forced-bias algorithm is used to resolve overlaps of the dilated spheres. The effect of this procedure on the aggregate geometry is illustrated in Fig. 3 c).

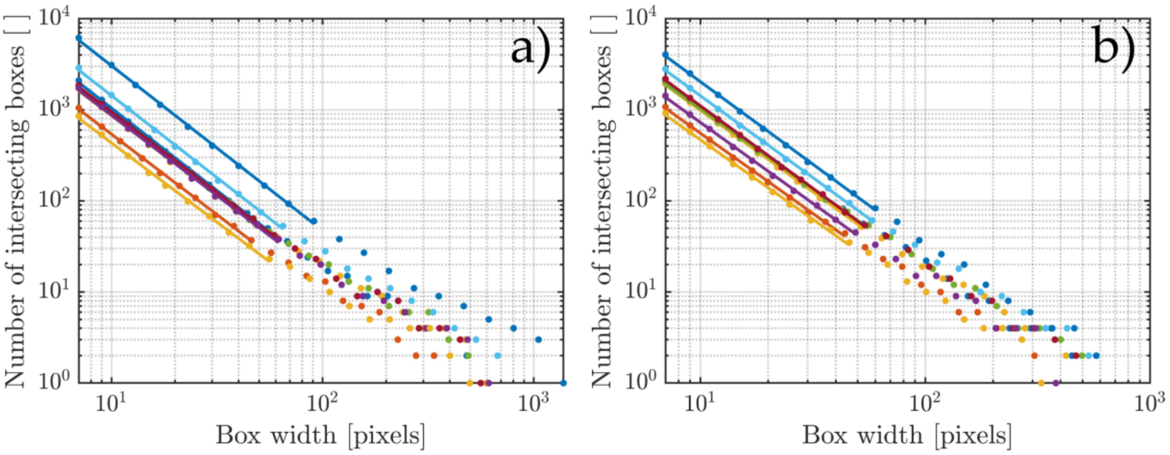

Fig. 4 Results of the box-counting method for a) measured aggregates and b) virtual aggregates. Each colour represents one measured aggregate and its corresponding virtually generated 3D aggregate. Scatter points denote the number of boxes intersecting the aggregate as a function of box size. Solid lines indicate the corresponding slopes.

2.2.2 Particle size distribution of LFP and LIC

The particle size distribution of the dispersed starting materials LFP and LIC was determined using laser light diffraction (device: Helos Vario KR, Sympatec). The measurement was performed directly behind the outlet of the brush dispersers in order to determine the PSD of the materials immediately after dispersion in the free jet and to use it as an input variable for the simulations carried out in this work. A detailed description of the measurement setup and the measurement technology used is provided in (Witte et al., 2025). During the measurements, the brush dispersers were operated at a feed rate of $500\ \mathrm{mm/h}$ and an inlet pressure of 2.5 bar. Six individual measurements were performed to verify reproducibility. To ensure high measurement accuracy, a minimum optical concentration of 5% was specified as a measurement condition.

Fig. 5 shows the number-based particle size distribution of LFP and LIC determined using laser light diffraction. Both powders predominantly contain particles in the sub-micrometre range. A comparison of the number-based median values shows that LIC, with $d_{50,0} = 0.68\ \mu\mathrm{m}$, contains slightly finer particles than LFP, with $d_{50,0} = 0.85\ \mu\mathrm{m}$. In the simulations, the maximum LIC particle size was constrained to $3\ \mu\mathrm{m}$, which can be realized in experiments through the implementation of a gas cyclone into the process (Zhao and Su, 2018). Fig. 5 also shows the aggregate size distribution of CB, resulting from the aggregate reconstruction methodology.

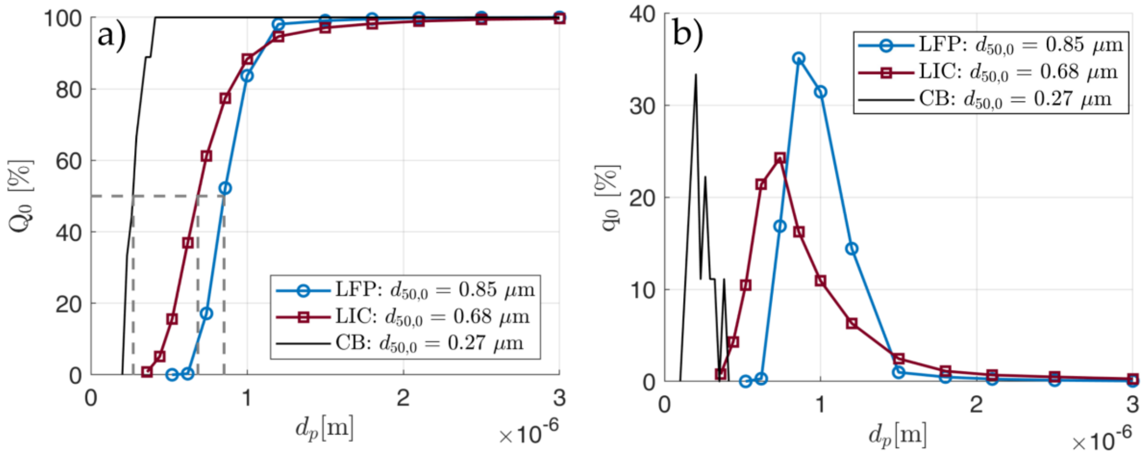

Fig. 5 a) Cumulative particle size distribution and b) particle size density distribution of LFP, LIC and CB. The dashed lines indicate the median diameter $d_{50,0}$.

2.2.3 Surface energy

The surface energy of the materials γ_s was determined from contact angle measurements using the Owens-Wendt-Rabel-Kaelble (OWRK) method (Kaelble, 1970; Owens and Wendt, 1969; Rabel, 1971). For this, contact angle measurements (see Fig. 6 a)) were performed using the capillary rise method with a DCAT 25 tensiometer (DataPhysics Instruments, Germany). For each measurement, 2.5 g of LFP, 2.5 g of LIC or 0.35 g of CB were filled into the measurement cylinder to carry out three to five measurements on each material with each test liquid (hexane, acetone, propanol, glycerine, thiodiglycol). The mass m of the test liquid drawn into the powder bed was recorded as a function of time t, and the squared mass m^2 was plotted against time (see Fig. A2 in the Appendix). Hexane was used to determine the capillary constant c (assuming a contact angle of 0°) and the other contact angles were derived from different test liquids by rearranging the equation

$$\frac{m^2}{t} = \frac{\gamma_\mathrm{L} \cdot \cos(\theta) \cdot \rho^2 \cdot c}{2 \cdot \eta} \,, \tag{25}$$

which is based on the Lucas-Washburn equation (Kühn et al., 2025; Lucas, 1918; Washburn, 1921). Here, the material data of the test liquids, such as the density ρ, viscosity η and surface energy γ_L were taken from the manufacturer's specifications at a temperature of 293.15 K. From the different contact angles, the linearized OWRK plots were generated (see Fig. 6 b)). In accordance with the methodology outlined in (Kühn et al., 2025), the OWRK plots were then used to determine the y-axis intersection as well as the slope. The polar γ_s^p and disperse part γ_s^d of the surface energy were then derived from

$$\frac{\gamma_\mathrm{L} \cdot (1 + \cos(\theta))}{2 \cdot \sqrt{\gamma_\mathrm{L}^\mathrm{d}}} = \sqrt{\gamma_\mathrm{s}^\mathrm{d}} + \sqrt{\gamma_\mathrm{s}^\mathrm{p}} \cdot \sqrt{\frac{\gamma_\mathrm{L}^\mathrm{p}}{\gamma_\mathrm{L}^\mathrm{d}}} \,, \tag{26}$$

where $\gamma_\mathrm{L}^\mathrm{d}$ and $\gamma_\mathrm{L}^\mathrm{p}$ correspond to the disperse and polar components of the test liquid also taken from the manufacturer's specifications.The resulting surface energies γ_s calculated as γ_s^p+γ_s^d were determined to be $19.15\,\mathrm{mJ/m^2}$ for LFP, $55.85\,\mathrm{mJ/m^2}$ for LIC, and $23.38\,\mathrm{mJ/m^2}$ for CB. Two remarks should be made in this context. First, all measurements were carried out under dry-room conditions with a dew point of 213.15 K. Since ambient humidity has a significant influence on adhesion forces, this factor must be taken into account when interpreting the results. Second, during the contact angle measurements, only a very small mass increase over time was observed for LFP and CB with water, and for LIC with thiodiglycol. This indicates very limited wetting of the respective materials, which led to the determination of a contact angle of approximately 90°. However, in reality, the actual contact angle may be even higher, a limitation that cannot be accurately captured using the Washburn method and should be verified using complementary Atomic Force Microscopy (AFM) measurements in the future (Kühn et al., 2025).

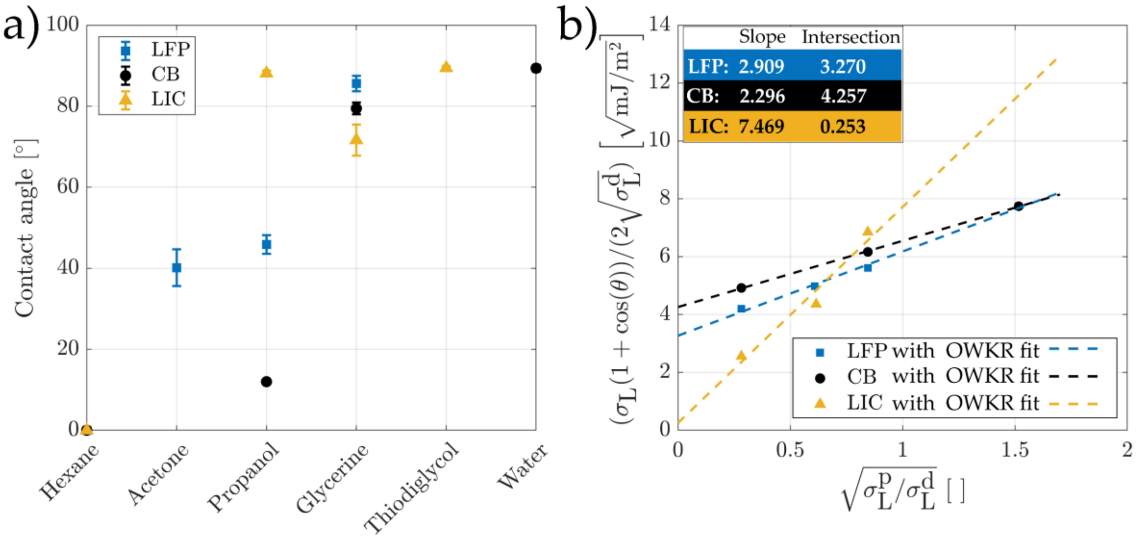

Fig. 6 Determination of the surface energy of the raw materials. a) Contact angle measurements and b) linear fit of the OWRK method for surface energy determination, where $\sqrt{\gamma_s^d}$ corresponds to the intersection with the ordinate and $\sqrt{\gamma_s^p}$ corresponds to the slope of the graphs.

3 Simulation setup

The objective of this work is the analysis and optimization of the gas phase-based formation of ASSB cathode hetero-agglomerates comprising LFP as active material, LIC as solid electrolyte and CB as conductive additive. The requisite material properties needed for the simulations are obtained from the literature and characterized experimentally, as described in Section 2.2. The necessary material properties, pertaining to both the starting materials and the pipe wall, are tabulated in Table 1.

Table 1 Material properties. "–" indicates parameters not required in the present model.

	Particle material			Wall material
Property	LFP	LIC	CB	Aluminium (Al) (Hornbogen et al., 2019; Parker et al., 2003)
Density ρ [kg/m^3]	3600 (Jeong et al., 2015)	2680 (Cheng et al., 2021)	1860 (Spahr et al., 2011)	–
Young's modulus Y [GPa]	47.3 (Sedlatschek et al., 2022)	38 (Molaiyan et al., 2023)	80 (Jean et al., 2011)	7.2
Poisson ratio ν [–]	0.28 (Maxisch and Ceder, 2006)	0.27 (Cheng et al., 2021)	0.3 (Jean et al., 2011)	0.34
Surface energy γ [mJ/m²]	19.15	55.85	23.38	1940

The proposed gas phase hetero-agglomeration process comprises three principal stages: first, the deagglomeration of the three starting materials; second, the subsequent mixing of the primary particles; and third, a turbulent pipe flow where larger agglomerates have time to form. The deagglomeration process entails the dispersion of the primary particles / aggregates in the gas phase and the feeding units require a specific amount of gas, which determines the gas volume flow rate in the pipe flows. The main mass in the composites, represented by LFP and LIC, is deagglomerated by feeding units, as presented in (Witte et al., 2023). The conductive additive CB present in primary aggregates represents only a very small amount of the composite mass and is therefore dosed by a smaller unit, providing only ¼ of the gas volume flow that is needed for each of the other materials. In considering a ternary system, it becomes evident that the various combinations of sequential mixing as well as direct mixing of the three materials may result in hetero-agglomerates of differing structures and quantities. Hence, it is aimed to analyse all potential combinations of mixing and agglomeration of the starting materials in turbulent pipe flows. Previous studies have demonstrated the significant impact of pipe diameter on hetero-agglomeration (Kolck et al., 2026). Consequently, the ternary process is aimed to be optimized concurrently with a view to facilitating the formation of hetero-contacts and controlling the size and quantity of formed agglomerates.

Four distinct simulation sets are utilized for the analysis and optimization of the ternary hetero-agglomeration process (see Fig. 7), wherein the optimization results of the second set and the premixing outflow simulation data of the third set are employed for the fourth set.

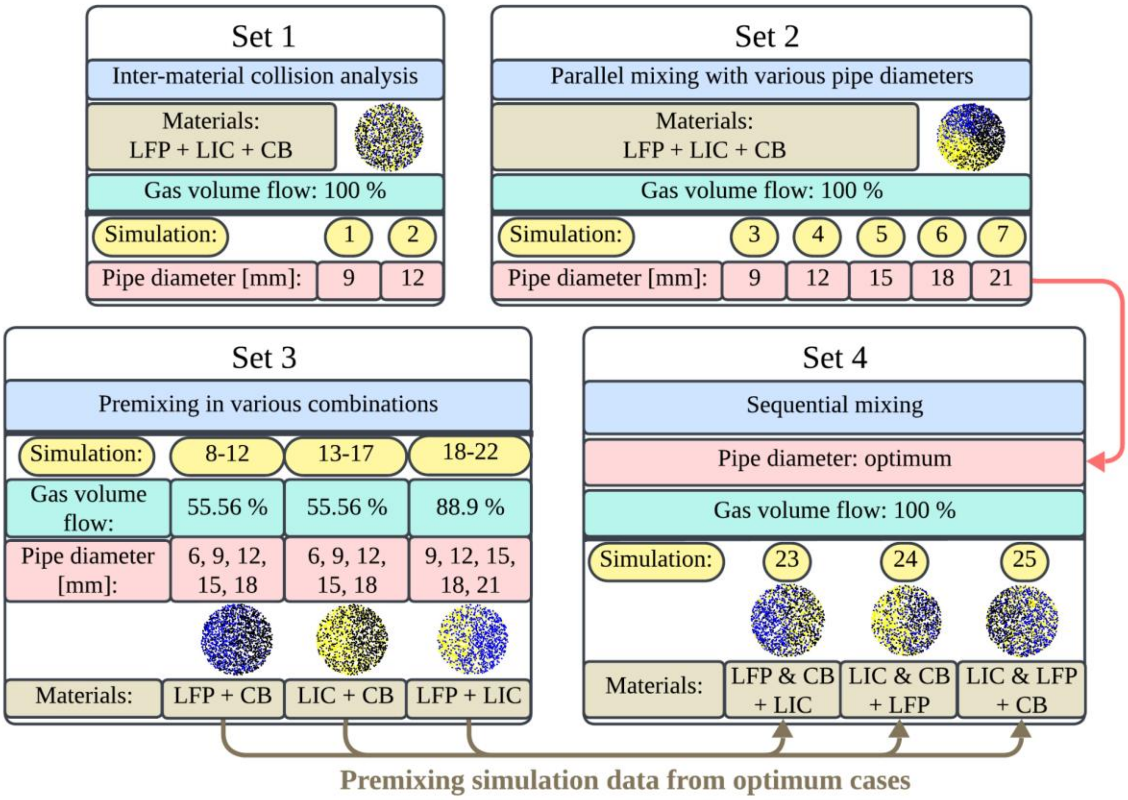

Fig. 7 Simulation workflow for modelling hetero-agglomeration in different mixing combinations.

A preliminary simulation set (Set 1) is conducted to ascertain the contributions to the collision kernel (i.e., the fundamental collision kernel, the accumulation effect and the collision efficiency) in Eq. (7) and the resulting collision frequency for each material combination of primary particles and aggregates. The analysis of the collision frequency between each material pair can subsequently be used to interpret the results of the other simulation sets. In this set, the particles and aggregates of all three materials are distributed uniformly across the pipe cross-section, i.e. considered as perfectly mixed, and the evaluation is conducted at the initial time step. In this set, two distinct pipe diameters are considered ($D_{\text{pipe}} = 9$ and $12\ \text{mm}$), which is regarded as sufficient for illustrating all trends while still obtaining clear results in a similar order of magnitude. The initial LFP and LIC particles are generated in accordance with the experimentally measured PSD (see Section 2.2.2) and the CB is introduced in the form of reconstructed aggregates (see Section 2.2.1). The total mass generated is determined by the solid mass flow, the volume of the simulation domain, and the gas volume flow (see Table 2).

Table 2 Two-phase flow and sequential section model parameters for all simulations.

Simulation	Pipe diameter [mm]	Volume flow [m^3/h]	Particle/aggregate mass flow [g/h]			
			LFP	LIC	CB	Sum
1-2	9, 12	7.875	145	95	10	250
3-7	9, 12, 15, 18, 21	7.875	145	95	10	250
8-12	6, 9, 12, 15, 18	4.375	145	/	10	155
13-17	6, 9, 12, 15, 18	4.375	/	95	10	105
18-22	9, 12, 15, 18, 21	7.000	145	95	/	240
23	Opt. Sim. 3-7	7.875	Opt. Sim. 8-12	95	Opt. Sim. 8-12	/
24	Opt. Sim. 3-7	7.875	145	Opt. Sim. 13-17	Opt. Sim. 13-17	/
25	Opt. Sim. 3-7	7.875	Opt. Sim. 18-22	Opt. Sim. 18-22	10	/

A second set of simulations (Set 2) is performed for the evaluation of the ternary mixing process of all three materials being mixed simultaneously, as opposed to employing a premixing process. The positions of the materials are azimuthally shifted from each other, imitating the merging of three particle-laden gas streams. As outlined in (Kolck et al., 2026), the particles are positioned at random radial locations, with the radial position expressed as $r_{\text{rand}} = \sqrt{RN}\;0.9\;D_{\text{pipe}}$, where RN is drawn randomly from the interval [0 1], and the position angle is determined by a random number drawn from a Gaussian distribution, here with a variance of $\pi/3$ for all materials and a material-dependent mean value of $2\pi/3$, $4\pi/3$ and 2π. The second simulation set has been designed to identify the optimal pipe diameter for the general ternary mixing process (all materials, 100% gas volume flow). This objective is to be realized through a thorough analysis of the parallel mixing process in Set 2. The findings from this analysis will be applicable to all simulations in Set 4, where the gas volume flow remains constant and the materials under consideration are consistent. The assessment of the optimum pipe diameter is contingent on the interplay of agglomeration and deposition, and is therefore primarily determined by the materials and the flow Reynolds number, both of which are equal for Set 2 and Set 4. The optimal outcomes of Set 2 will be compared with the results of Set 4, which encompasses all premixing combinations in pipe flows with the respective diameter. The pipe diameter dependency of the three-component mixing, hetero-agglomeration and deposition as part of simulation Set 2 is evaluated by considering five different pipe diameters ($D_{\mathrm{pipe}} = 9, 12, 15, 18$ and $21\ \mathrm{mm}$), which correspond to pipe flow Reynolds numbers of $21196, 15897, 12718, 10598$ and 9084, respectively. The maximal axial particle distance, i.e., the pipe length, was set to $3.5\ \mathrm{m}$ for all simulations.

A third simulation set (Set 3) is conducted for the simulation of the binary premixing of the three different starting materials in various combinations (LFP with CB, LIC with CB and LFP with LIC). Here again, the initial particles and aggregates are set within the inner 90% of the pipe cross-section and with a lateral displacement that imitates the particle distribution resulting from the merging of two particle-laden gas flows. In this set, the mean azimuthal angle is set to π for one material and 0 for the other (Kolck et al., 2026). The initial particles and aggregates are generated in accordance with the procedure outlined for simulation Set 2. Since the quality of the premixing is expected to depend on the pipe diameter as well, each combination is simulated for five different pipe diameters. The premixing combinations involving CB are characterized by a reduced volume flow (one large and one small feeding unit) and consequently necessitate the consideration of slightly smaller pipe diameters ($D_{\mathrm{pipe}} = 6, 9, 12, 15$ and $18\ \mathrm{mm}$). In contrast, the premixing of LFP and LIC is to be analysed for larger pipe diameters corresponding to those of Set 2 ($D_{\mathrm{pipe}} = 9, 12, 15, 18$ and $21\ \mathrm{mm}$), as it proceeds with a larger volume flow resulting from the deagglomeration in two large feeding units. The objective is to identify the optimal premixing result for each material combination in terms of the mixing, and deposition. In contrast to the other sets, the simulations of Set 3 are terminated when either the predefined global Lacey mixing index of $M_{\mathrm{G}} = 0.98$ (Kolck et al., 2026; Lacey, 1954) is attained, or when an axial particle distance of $2\ \mathrm{m}$ is reached. At this phase, the particle systems are considered sufficiently mixed. For each premixing combination, the outflow particles and agglomerates from the simulation results deemed most optimal are then transferred as input data to Set 4.

In the fourth simulation set (Set 4), particles and agglomerates originating from the optimum premixing simulation results are initially set laterally shifted to the newly generated missing material particles and aggregates. These were generated and placed in accordance with the initialization methodology employed in all simulations of Set 3. The incorporation of the missing material at the initiation of the simulation in Set 4 occurs at the pipe distance at which the respective premixing simulation was terminated. In contrast to the simulations conducted in the framework of the third set, these simulations do not terminate upon reaching a desired state of mixing, but at a fixed pipe length of $L_{\mathrm{pipe}} = 3.5\ \mathrm{m}$. The fourth simulation set aims to model the main hetero-agglomeration process for all premixing combinations in order to compare it with the simultaneous mixing of Set 2.

All simulations are conducted with gas volume flows and solid mass flows that originate from practical conditions (see Table 2). The gas volume flow is selected based on the ideal gas volume flow used for dispersing in the feeding units. Previous studies have demonstrated that the optimum flow rate for one large feeding unit used for the dispersion of LFP and LIC is $3.5\ \mathrm{m}^3/\mathrm{h}$ (Witte et al., 2023). This value represents an optimal balance between effective agglomerate breakup of the starting materials and sufficient particle concentration to facilitate effective hetero-agglomeration. The gas volume flow of $7.875\ \mathrm{m}^3/\mathrm{h}$ (denoted as 100 % in Fig. 7) applied in Sets 1,2 and 4 is derived from the dispersing gas volume flow of two large feeding units for the respective deagglomeration of LFP and LIC, as well as from that of the smaller feeding unit, which is only ¼ of the larger volume flow and is used for the deagglomeration of CB. Following this principle, the volume flow of simulations 8-17 is derived from one large and one small feeder (55.56%) and that of simulations 18-22 is derived from two large feeders (88.9%). The mass flow tabulated in Table 2 is derived from a desired material ratio of 4% CB, 38% LIC and 58% LFP (Frankenberg et al., 2024) with a total solid mass flow of $250\ \mathrm{g}/\mathrm{h}$, which was found to allow for reasonable deagglomeration of the starting materials.

4 Results

4.1 Simulation set 1: Inter-material collision analysis

Prior to the analysis of the overall hetero-agglomeration process of all materials, it is essential to comprehend the collision mechanisms between particles of the same and different materials. As discussed in Section 2.1.2, the collision rate is determined by the collision kernel given by Eq. (7). The collision kernel of two particles Γ_{ij} is the product of the fundamental, spherical collision kernel $\Gamma_{ij,0}$, the RDF g_{ij} and the collision efficiency β_{ij}, the meaning of which has been discussed earlier. Each of these factors is unique to each particle collision combination, thereby resulting in different agglomeration rates. Hence, it is aimed to ascertain the manner in which these factors contribute to the collision rate for each material pair combination and how these factors change when the pipe diameter is varied (for example, when D_{pipe} is set to $9\ \mathrm{mm}$ and $12\ \mathrm{mm}$). Consequently, the collision kernel and all contributors between each real and its fictitious particle/aggregate have been evaluated in the initial simulation step. The values have been organized according to the material combination (LFP-LFP, LIC-LIC, LFP-LIC, LFP-CB and LIC-CB) and averaged. It should be noted that CB-CB collisions are not considered in this analysis due to their negligibly small kernels and radial distribution functions. The results are presented in Fig. 8 as a function of the normalized pipe radius $\tilde{r}$.

The material-combination dependent mean RDF $\overline{g}$ shown in Fig. 8 a) describes the accumulation effect for particles with a Kolmogorov Stokes number close to one. It can be observed that the accumulation effect is very strong for LFP particles in the case of smaller pipe diameters. This phenomenon can be attributed to the larger response time of these particles, which is associated with their greater density and larger median particle size. Close to the wall, where eddies are small (i.e., small Kolmogorov time scales), turbulent fluctuations are large and the turbulent Reynolds number is high, the radial distribution function exhibits a peak for all material combinations. For the more inert LFP, the mean collision kernel can be increased by up to a factor of 11 through the accumulation effect. The LIC particles are less inert and have smaller Kolmogorov Stokes numbers. However, for smaller pipe diameters, the mean values of the RDF still reach values of up to 5. The radial distribution function of LFP and LIC particles is similar to that of LIC particles colliding with each other, but shifted slightly to larger values. This demonstrates that the accumulation effect primarily influences the collision rate between two particle classes through the radial distribution function of the lower accumulating class. The radial distribution function of collisions involving carbon black is negligible, due to the very large responsive behaviour of these particles, which results in no local preferential concentration. When the pipe diameter is increased, the accumulation effect of all material pairs is strongly reduced. This is due to the larger Kolmogorov time scales and consequently smaller Kolmogorov–Stokes numbers observed in larger pipes. However, the accumulation effect is still significant, particularly when considering LFP-LFP collisions, and can increase the fundamental collision kernel by more than a factor of three.

The material-combination dependent mean collision efficiency $\bar{\beta}$ between each material pair is presented in Fig. 8 b). In the majority of cases, collisions between and among the LFP and LIC particles result in impingement. Furthermore, the influence is not significant even in the case of a larger pipe radius. This is because of the comparatively similar size ratio of the collision partners. From Eq. (18), it can be deduced that the collision efficiency due to interception is one in the limit of zero collector Reynolds number, provided that the diameter of the impinging particle is larger than half of that of the collector particle. It is notable that this critical ratio decreases further when finite collector Reynolds numbers are taken into consideration. Furthermore, the inertial collision efficiency also plays a significant role in many collisions. Conversely, collisions between the carbon black aggregates and the larger LFP and LIC particles frequently do not result in impingement, as evidenced by lower collision efficiencies. In such cases, the interception mechanism remains the most significant contributor, with the effect of Brownian motion providing a marginal support of approximately 10%. Due to the fact that the carbon black aggregates exhibit minimal response times, the collision efficiency resulting from inertial impaction is generally negligible. The disparity in collision efficiency between LFP-CB collisions and LIC with CB can be attributed to the smaller size of the LIC particles, resulting in larger size ratios and, consequently, an increased interception collision efficiency. Increasing the pipe diameter slightly reduces the collision efficiency of LFP-CB and LIC-CB collisions, which is due to the smaller collector Reynolds numbers resulting from lower collision velocities.

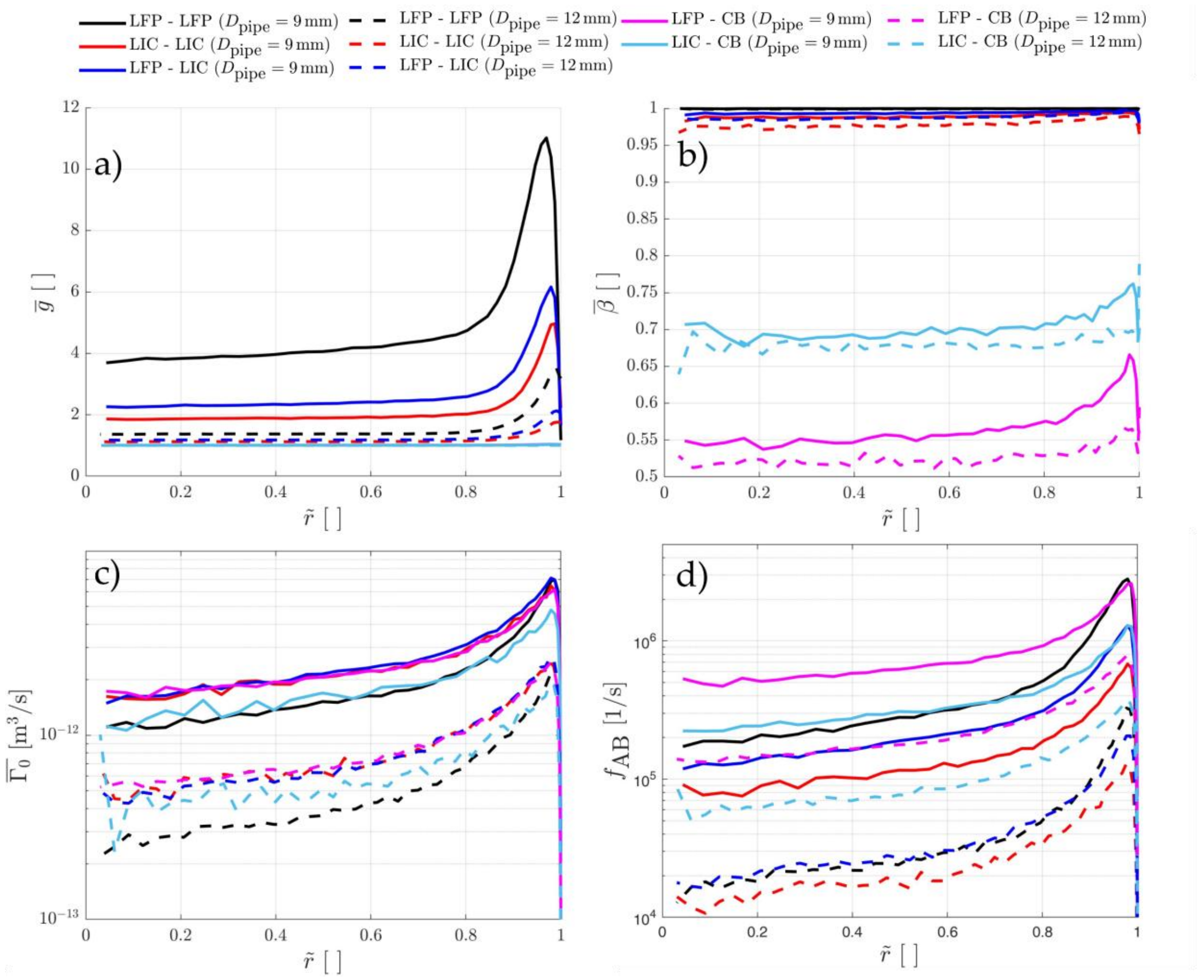

Fig. 8 Mean material-pair collision kernel contributions and resulting collision frequency. The plots show a) the mean radial distribution function, b) the mean collision efficiency, c) the mean fundamental collision kernel and d) the collision frequency as a function of the normalized pipe radius $\tilde{r}$. The data is presented for a pipe diameter of $D_{\mathrm{pipe}} = 9\mathrm{mm}$ (solid line -) and $D_{\mathrm{pipe}} = 12\mathrm{mm}$ (dashed line - -).

The mean fundamental inter-particle collision kernel $\overline{\Gamma_0}$ for different material combinations is shown in Fig. 8 c) as a function of the normalized radius. A peak close to the wall is evident for all combinations, which is attributed to the larger Stokes numbers in this region. The collision kernels of LIC-LIC, LFP-LIC and LFP-CB are very similar at almost every radial pipe position. In contrast, the LFP-LFP collision kernel is smaller in most regions, only exhibiting similar values at the near-wall peak. This can be attributed to the narrower particle size distribution of LFP (see Fig. 5), which leads to smaller differences in Stokes numbers. Consequently, the accelerative collision mechanism is reduced due to distinct response times. In contrast, LIC particles exhibit a broader size distribution and consequently a broader inertial response. This large difference in inertial response also explains the large collision kernel observed between LFP and CB, as well as between LIC and CB. As the mean LFP particle is heavier due to its size and density, the difference in Stokes number between it and the CB aggregates is greater. This results in a larger collision kernel than collisions involving LIC and CB.

Furthermore, it has been demonstrated that an increase in pipe radius results in a significant shift of the mean collision kernel towards lower values. This phenomenon can be attributed to the reduction in turbulent fluctuations. At this point, it is essential to emphasize that the collision rate provides information regarding the number of collisions that occur in a specified time interval. In the context of pipe flow, it is imperative to acknowledge that an increase in pipe radius invariably results in a corresponding increase in residence time. This indicates that the variation in collisions per pipe length interval is less pronounced than the variation in collision rate. Furthermore, it is noteworthy that the augmented peak of LFP-LFP collisions, which has been observed for $D_{\mathrm{pipe}} = 9\ \mathrm{mm}$, is not evident for $D_{\mathrm{pipe}} = 12\ \mathrm{mm}$. This finding suggests that the augmented LFP-LFP peak can be attributed to inertial collisions for particles with larger Stokes numbers, while other collisions are predominantly driven by variations in Stokes numbers. However, in the case of larger pipe radii, this effect is no longer observable due to the reduced turbulence and the presence of very small Stokes numbers for all particles. It can thus be concluded that all collisions are primarily driven by the accelerative mechanism. As a consequence, the LFP-LFP collision kernel is smaller than the LFP-LIC and LIC-LIC collision kernel over the entire pipe radius.

It is evident that the actual collision probability P_{ij} is not solely determined by the collision kernel, but also by the number of particles (see Eq. (6)). It is therefore imperative to consider the collision frequency between materials A and B, given the disparity in the number of particles and aggregates for each material:

$$f_{AB} = \frac{1}{V_{\mathrm{pipe}}} \sum_{i \in I_A} \sum_{j \in I_B} \Gamma_{ij,0}\, g_{ij} \beta_{ij}, \qquad (27)$$

where V_{pipe} is the volume of the considered pipe section and I_A and I_B are the sets of all parcels of material A and B, respectively. The collision frequency is evaluated at each radial pipe position, with the results shown in Fig. 8 d). The collision frequency of LFP with CB is observed to be the highest over the entire radius of the pipe. This phenomenon can be attributed to the large collision kernel and the high number of CB aggregates and LFP particles present. The collision frequency between LFP particles is generally lower, as there are far fewer LFP particles than CB aggregates. However, the LFP-LFP collision frequency exhibits similar values near the wall, primarily due to the large value of $\bar{g}$ in that region. Despite the substantial magnitude of the fundamental collision kernel for LIC-LIC and LFP-LIC collisions over the entire pipe radius (see Fig. 8 c)), the corresponding collision frequencies are considerably smaller. This is due to the smaller number of collision partners when compared to collisions involving CB, as well as the smaller accumulation effect of LIC particles. Furthermore, the number of LIC particles is much smaller than that of LFP particles, thereby also reducing the collision rate involving LIC particles.

While the collision rate of LFP particles is similar to that of CB particles for $D_{\text{pipe}} = 9\ \text{mm}$, this is not evident for $D_{\text{pipe}} = 12\ \text{mm}$ because the accumulation effect is small for every material in that case. In contrast to the smaller pipe radius, the hetero-collision rate is similar to the LFP collision rate. It can therefore be deduced that, for pipes with smaller diameters, collisions between and among LFP and LIC particles play a more significant role than in the case of larger diameters, where the agglomeration of LFP or LIC particles with CB aggregates is predominant.

4.2 Simulation set 2: Parallel mixing and determination of the optimal pipe diameter

As demonstrated in Section 4.1, the collision rates of all materials exhibit a substantial decrease with an increase in pipe diameter. However, it is imperative to consider the effect of rebound and adhesion, agglomerate growth and deposition when assessing the suitability of pipe diameters for the proposed process, given the specified process and material conditions.

In this section, the overall agglomeration result is considered in order to determine the diameter to be used in Set 4.

Fig. 9 shows the axial evolution of the LFP/LIC particle and CB aggregate fraction being captured in non-deposited agglomerates for all pipe diameters under consideration. It is important to note that CB-CB clusters which do not contain an LFP or an LIC particle are not considered agglomerates in this study for reasons of clarity. It is evident that, due to the large number of CB aggregates, even in the event of a negligible proportion of CB aggregates agglomerating with one another, there will be a substantial augmentation in the number of agglomerates, whilst concomitantly providing no information about the desired large-scale, multi-component agglomerates.

Fig. 9 demonstrates that the initial agglomeration rate, indicated by the slope of the graphs, decreases with increasing pipe diameter. This finding aligns with the observations presented in Section 4.1. However, these slopes do not decrease as strongly as the collision frequency in Fig. 8 d) with increasing pipe diameter. This is because particles in larger pipes have longer residence times, thereby increasing the number of collision events in a specific pipe interval. Moreover, in the case of the smallest pipe diameter, most collisions between and among LFP and LIC particles do not result in agglomeration due to rebounding. Conversely, in the simulation of the broadest pipe, each collision results in agglomeration. However, the agglomeration of LFP and LIC particles is not initially dominant with respect to the fraction being captured in agglomerates. As was discussed in Section 4.1, the majority of collisions occur between the large primary particles and the CB aggregates (see Fig. 8 d)).

Although smaller pipes lead to stronger agglomeration of all materials, pipes with a larger diameter generally have the potential to capture larger fractions of all materials in agglomerates. As the pipe diameter increases, deposition decreases, increasing the length of the pipe at which the maximum number of LFP and LIC particles are captured in non-deposited agglomerates (indicated by the dashed lines in Fig. 9). This increases the residence time and the corresponding overall collision number. For the largest pipe diameter, the maximum is reached immediately prior to the termination of the pipe, whereas for the smallest diameter, the maximum is found at a very low axial distance ($x_{\mathrm{pipe}} = 0.4, 0.86, 1.45, 2.73$ and $3.45\ \mathrm{m}$ for $D_{\mathrm{pipe}} = 9, 12, 15, 18$ and $21\ \mathrm{mm}$, respectively). The number of free agglomerates and the bounded particles therein decreases rapidly. Due to their large inertia and the strong fluctuation velocities, larger agglomerates, which contain more primary particles, are deposited particularly frequently. Conversely, due to the smaller RMS velocities, larger agglomerates are more effectively retained in the main flow with larger pipe diameters.

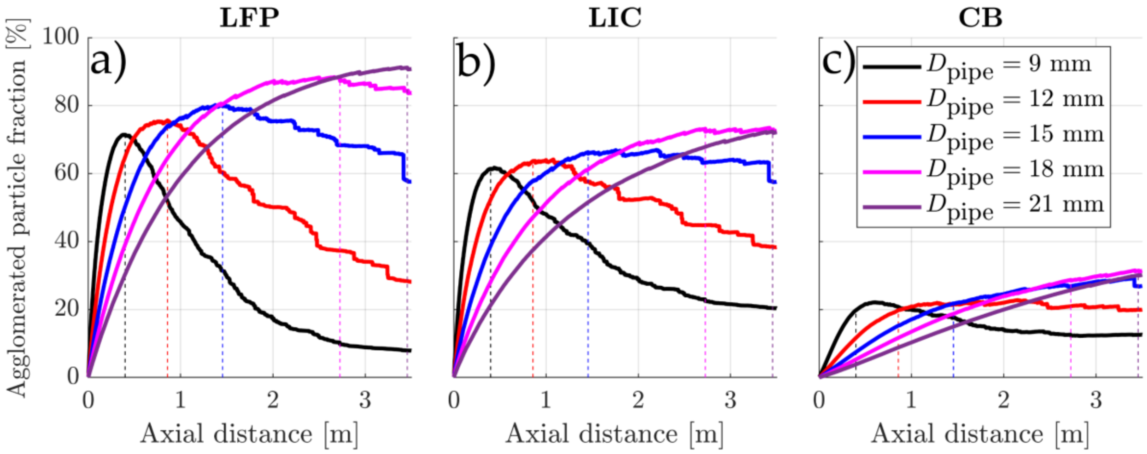

Fig. 9 Fraction of a) LFP, b) LIC and c) CB particles being captured in non-deposited agglomerates over the axial particle distance for different pipe diameters. The dashed lines indicate the distances at which the maximum values of LFP and LIC particles captured are observed in the respective pipe.

This observation is underlined by Fig. 10 a), which illustrates the mean and mass-weighted mean LFP/LIC particle and CB aggregate number per agglomerate. From an engineering perspective, the mass-weighted mean number provides a more informative metric, as it reflects the distribution of the composite mass. The mass-weighted mean particle/aggregate number per agglomerate has been shown to increase with increasing pipe diameter, reaching a maximum at a pipe diameter of $D_{\mathrm{pipe}} = 18\ \mathrm{mm}$. In the case of $D_{\mathrm{pipe}} = 21\ \mathrm{mm}$, the residence time is inadequate for achieving comparable values, at least in the case of a limited pipe length. The phenomenon of larger and heavier agglomerates being observed in larger pipes can again be explained by the decreased large-agglomerate deposition in such instances. Furthermore, particle and agglomerate breakup can be observed in the case of very small pipe diameters, which is caused by the higher collision velocities (in particular for larger agglomerates). Consequently, agglomerate growth is attenuated in this case.

In addition to the large, massive agglomerates, there are numerous small agglomerates, some of which consist solely of an LFP/LIC particle and a few CB aggregates. Hence, the mean values presented in Fig. 10 a) are considerably smaller in comparison to the mass-weighted mean. It is evident that a considerable number of agglomerates are devoid of LIC particles, thereby resulting in a mean LIC number per agglomerate that is less than one for all cases. Local maxima in mean values of all LFP and LIC can be found for $D_{\text{pipe}} = 9\ \text{mm}$ and a maximum mean CB number is observed for $D_{\text{pipe}} = 21\ \text{mm}$. This finding suggests that, in the case of the smallest pipe diameter, smaller agglomerates consist of more particles, while very large agglomerates are less common. This underlines the large-agglomerate deposition and agglomerate breakup, causing mass loss and poorer agglomerate growth, respectively. It can be observed that the mean CB aggregate number is significantly higher than the mean number of LFP or LIC particles. This observation can be attributed to the fact that, despite the CB mass fraction being a mere 4%, there are more than 17 and 13 CB aggregates in the system for every LIC and LFP particle, respectively.

As outlined in (Kolck et al., 2026), the ratio of hetero-contacts to homo-contacts (RHH) in a system is contingent on the pipe diameter, given that the critical collision velocities and the underlying surface energies of the materials differ significantly from one another. This dependency can be attributed to the variation in collision velocity when varying the pipe radius. Fig. 10 b) shows the ratio of LFP-LIC contacts to LIC-LIC and LFP-LFP contacts at the point of maximum LFP and LIC capturing for all pipe diameters under consideration. In the case of smaller pipe diameters, most of the hetero collisions do not result in agglomeration, since the prevalent collision velocities are larger than the critical collision velocities. However, a greater proportion of LFP-LFP collisions result in agglomeration, thereby leading to a reduced RHH. Increasing the pipe diameter reduces collision velocities, allowing more hetero-collisions to result in agglomeration. In addition, differences in mixing can enhance this phenomenon, as poor mixing leads to an increased number of homo-collisions in a poorly mixed state. The dependence of mixing on pipe diameter will be discussed in Section 4.3.

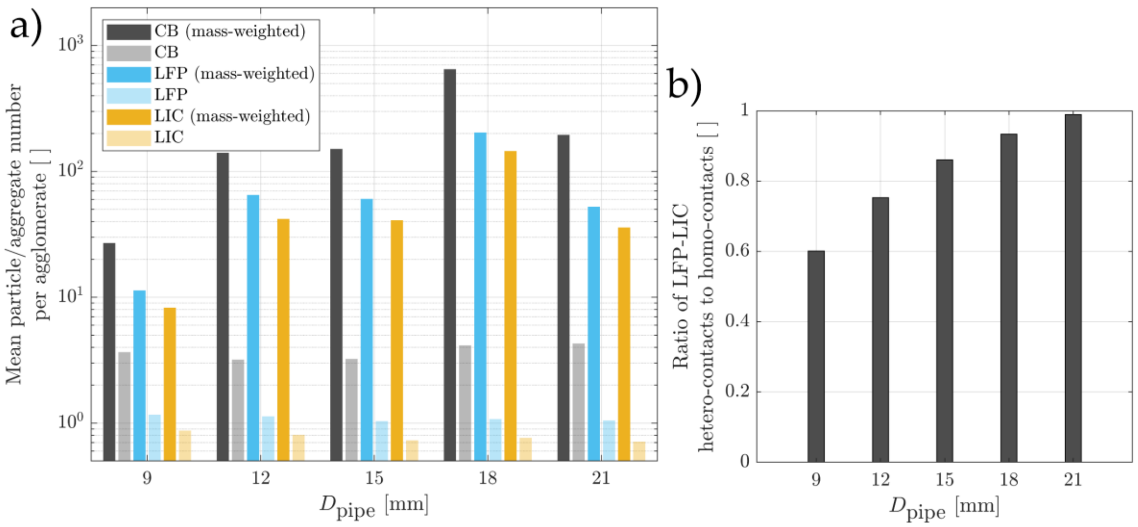

Fig. 10 a) Mean and agglomerate mass-weighted mean number of LIC and LFP particles and CB aggregates per agglomerate shown for different pipe diameters at the respective axial particle distances, at which the maximum number of LFP and LIC particles are captured in non-deposited agglomerates and b) ratio of LFP-LIC hetero-contacts to homo-contacts (RHH) shown for different pipe diameters at the respective axial particle distances, at which the maximum number of LFP and LIC particles are captured in non-deposited agglomerates.

It can be concluded from the consideration of the maximum number of particles captured in non-deposited agglomerates, the mean particle numbers and the associated agglomerate growth, as well as from the RHH, that larger pipe diameters are generally more suitable for the considered process and the given materials. In the selection of pipes with reduced diameter, it is imperative that the pipe length is sufficiently short in order to prevent substantial mass loss due to deposition. Conversely, the utilization of broader pipes necessitates sufficient length to augment the residence time required for optimal agglomerate growth. The simulation with $D_{\text{pipe}} = 18\,\text{mm}$ is selected for comparison against other mixing configurations as part of simulation set 4, where this diameter will also be applied. It should be noted that the mixing index and the distribution of contacts within the agglomerates resulting from this case will be analysed in Section 4.4. This will allow for a comparison of the results with those obtained from different mixing configurations. As demonstrated in Fig. 9, the maximum number of captured particles is marginally smaller than that resulting from the largest diameter. However, the formed agglomerates are substantially larger, exhibiting a comparable ratio of hetero-contacts to homo-contacts. In the case of $D_{\mathrm{pipe}} = 21\ \mathrm{mm}$, it is evident that the pipe would necessitate a greater length to yield larger agglomerates while maintaining a comparable fraction of agglomerated particles. Should experimental implementation permit significantly longer pipe lengths, this should be given consideration, as should the implementation of even larger pipe diameters.

4.3 Simulation set 3: Premixing of two materials

The premixing of LFP with CB, LIC with CB, and LFP with LIC is considered for pipe flows with five different diameters, in order to identify the conditions at which a mixed state is reached while preventing deposition. In Fig. 11 a), the axial mixing length, defined as the length of pipe required for nearly complete mixing ($M_{\mathrm{G}} = 0.98$), is presented as a function of pipe diameter for a limited pipe length of $2\ \mathrm{m}$. When considering the mixing of LFP with CB and LIC with CB, a proportionality between mixing length and pipe diameter is evident for $D_{\mathrm{pipe}} \geq 9\ \mathrm{mm}$. Increases in pipe diameter result in decreases in turbulent fluctuations and increases in radial and azimuthal mixing distances. Consequently, there is an observed decrease in mixing per axial distance. However, this effect is counteracted, at least in part, by an increase in residence time due to a decrease in mean flow velocity. It is noteworthy that this is not the case for $D_{\mathrm{pipe}} = 6\ \mathrm{mm}$ in both instances, where larger axial mixing distances are observed, although the pipe diameter is smaller. This is due to the fact that, in these cases, turbophoresis, the effect of particles migrating from regions of strong turbulence to regions of weak turbulence (Caporaloni et al., 1975; Reeks, 1983), becomes dominant. This phenomenon results in the capture of inertial (LFP or LIC) particles within the viscous sublayer, effectively segregating them from the CB particles, which do not undergo this effect due to their significantly smaller inertia. Consequently, a poor mixing state is sustained for a greater duration until the particles captured in the sublayer are deposited.

The deposition is illustrated in Fig. 11 b), where a deposition of 80 % and almost 60 % can be observed at the mixed state for LFP-CB and LIC-CB premixing, respectively. As the mean LFP particle mass is higher (i.e., they have larger Stokes numbers), the effect of turbophoresis and the resulting segregation is stronger in the case of LFP-CB premixing, resulting in a mixing length that is more than double that in the case of $D_{\mathrm{pipe}} = 9\ \mathrm{mm}$. In this instance, the minimum mixing length can be identified for both mixing cases. The mixing length of LIC with CB is comparable to that of LFP with CB; however, slightly smaller distances are required to reach a mixed state. This phenomenon can be attributed to the higher diffusivity of the LIC particles within the region of homogeneous turbulence, which also results in a faster onset of the deposition process. Although the deposition velocity of LFP is larger in the "diffusion-impaction" regime (Kolck et al., 2026; Sippola and Nazaroff, 2002), the higher diffusivity of LIC leads to deposition beginning at an earlier stage. This leads to an increased deposited mass at a mixed state (see Fig. 11 b), which is assisted by a higher LIC mass fraction deposition, attributable to a wider particle size distribution. In the case of LFP-CB premixing, minimal deposition is observed at the mixed state when $D_{\mathrm{pipe}} = 12\ \mathrm{mm}$. As this particular simulation case also permits rapid mixing, it has been selected for use in obtaining the premixing data required for Simulation 23. In the case of LIC-CB premixing, a mixing state with negligible deposition is reached for $D_{\mathrm{pipe}} = 15\ \mathrm{mm}$, which is therefore selected as the relevant premixing diameter for Simulation 24.

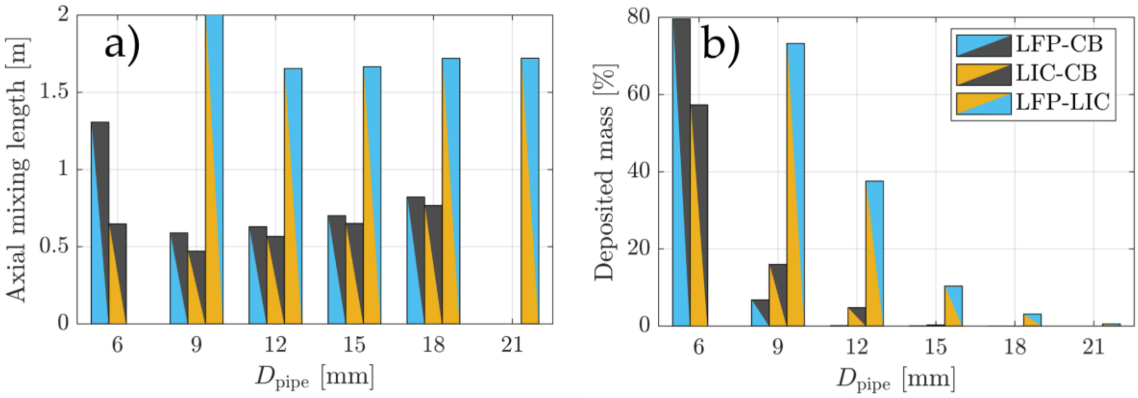

Fig. 11 a) Axial particle/agglomerate position at which a mixing state ($M_{\mathrm{G}} = 0.98$) is reached and b) deposited mass at mixing state for different pipe diameters D_{pipe} and different premixing combinations. Note that the variation in pipe diameter in the case of LFP-LIC premixing differs from that in the other cases.

The premixing of LFP and LIC generally necessitates larger pipe distances, which is attributable to a reduced diffusivity when compared to the premixing simulations involving small CB aggregates. Furthermore, the occurrence of longer mixing distances can be attributed to the dispersion of both materials into the viscous sublayer at opposite pipe sides, a phenomenon that is particularly evident in cases where the pipe diameter is reduced. In the case of $D_{\mathrm{pipe}} = 9\ \mathrm{mm}$, the effect is so pronounced that the mixed state attains a plateau at approximately $M_{\mathrm{G}} = 0.95$ at the terminal point of the pipe. At this stage, more than 70% of the initial mass is deposited. Turbophoresis has been observed to be less dominant for larger pipe diameters. Furthermore, the axial mixing length has been shown to reach a minimum for $D_{\mathrm{pipe}} = 12\ \mathrm{mm}$. However, 37% of the mass is deposited in this case. In order to ensure consistency with regard to the requirement of deposition avoidance, the simulation with $D_{\mathrm{pipe}} = 21\ \mathrm{mm}$ is selected for the purpose of obtaining the premixing simulation data for Simulation 25. In comparison with the simulation yielding the minimum mixing length, this mixing length is only approximately 4% longer, while avoiding 37% mass loss.

4.4 Simulation set 4: Three-component hetero-agglomeration with various premixing combinations

4.4.1 Pipe flow agglomeration and deposition

The three different sequential mixing configurations simulated in Set 4 are compared with the parallel mixing configuration (Simulation 6) by considering, once again, the axial evolution of the LFP/LIC particle and CB aggregate fraction being captured in non-deposited agglomerates (see Fig. 12). For the purpose of comparison, the results from Set 2 are also illustrated as shaded lines, ending at the mixed state distance, from which the subsequent simulation of Set 4 is initiated. In the case of premixing LFP with CB (Simulations 10 and 23), a significantly stronger LFP agglomeration can be observed for premixing and a smooth transition between the premixing and the subsequent mixing step is evident. This phenomenon can be attributed to two observations. Firstly, the carbon black concentration is considerably higher in the LFP-CB premixing configuration than in the parallel mixing configuration, which is due to a reduced gas volume flow (55.56%). Secondly, the agglomeration of LFP is primarily driven by LFP-CB collisions, as can be deduced from the collision frequencies shown in Fig. 8 d). In return, this phenomenon results in an augmentation of the agglomerated CB fraction, as demonstrated in Fig. 12 c), when compared to the parallel mixing configuration. It is evident that the agglomerated LIC particle remains at a constant level of zero until the initiation of the second mixing step. At this juncture, the process of LIC agglomeration starts, resulting in a graph that is analogous to the initial stage of the parallel mixing configuration, although exhibiting a marginally diminished slope. This observation can be attributed to the 13% CB that has already agglomerated on LFP particles at this stage. It is noteworthy that the axial distance, at which the number of LFP and LIC particles being captured in non-deposited agglomerates reaches a maximum, $2.45\ \mathrm{m}$, is less than that of the premixing simulation. At this stage, the number fraction of LFP being captured in free agglomerates is almost equal to that resulting from the parallel mixing simulations. In contrast, a significantly smaller proportion (only approximately 59%) of LIC is captured in non-deposited agglomerates. This phenomenon can be attributed to the fact that, in the case of LFP-CB premixing, a significant proportion (approximately 40%) of LIC particles remains free-moving and not yet agglomerated (see Fig. 13 b)), while LIC deposition remains minimal (see Fig. 13 a)). Conversely, at this stage, a substantial LFP fraction has already been deposited, with only approximately 3% of the LFP particles remaining as non-deposited primary particles. The elevated LFP deposition fraction is attributable to the presence of large agglomerates comprising LFP, which exhibit accelerated deposition velocities. In contrast, individual, non-agglomerated particles remain within the flow. In the case of parallel mixing, a comparable proportion of LIC and LFP has been deposited at this stage, as both materials are introduced concurrently and are captured into agglomerates that subsequently deposit.

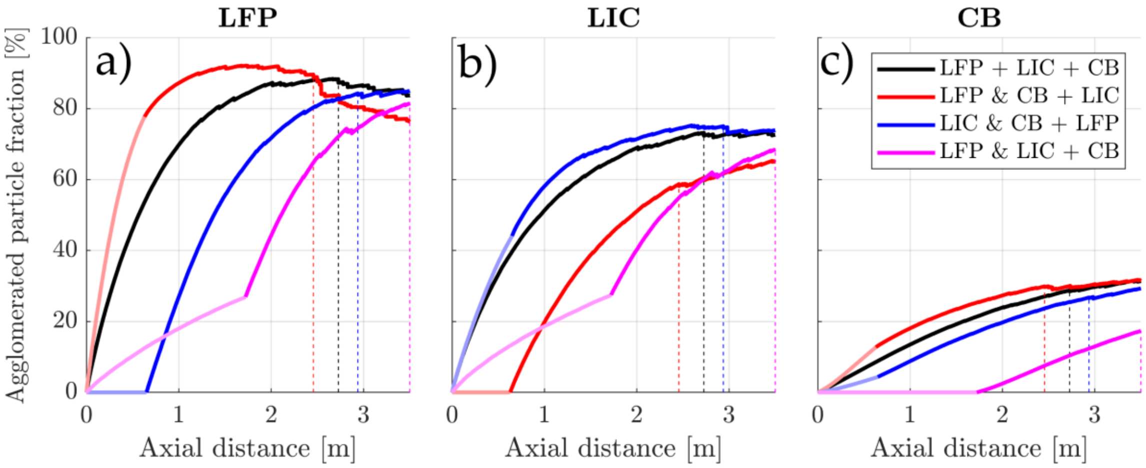

Fig. 12 Fraction of a) LFP, b) LIC and c) CB particles being captured in non-deposited agglomerates over the axial particle distance for different mixing combinations. The dashed lines indicate the distances at which the maximum values of LFP and LIC particles captured are observed in the respective configuration and the shaded lines indicate the results from the premixing simulation.

A similar, yet opposing behaviour can be observed in the case of LIC being premixed with CB. In this instance, the premixing LIC agglomeration demonstrates an increase in comparison to the parallel mixing case. However, this increase is not as significant as the LFP agglomeration increase of the LFP-CB premixing configuration that was discussed earlier. This phenomenon can be attributed to the observation that the presence of LFP plays a more significant role in the agglomeration of LIC than the other way around. This observation becomes evident when considering Fig. 8 d). The collision frequency of LFP-CB collisions is found to be significantly higher than the LFP-LIC collision frequency, while the graph of LIC-CB collisions exhibits a substantially smaller offset. This indicates that collisions with CB are predominant for both LFP and LIC. However, the ratio of LIC-LFP to LIC-CB collisions is significantly higher than the ratio of LFP-LIC to LFP-CB collisions. This observation is also reflected by the discontinuity in LIC agglomeration when LFP is introduced at the initial stage of the subsequent mixing stage, because the LFP plays a significant role in LIC agglomeration. The lower LIC-CB collision frequencies in comparison to the LFP-CB collision frequencies explain the differences in agglomerated CB fraction at the stage where the second mixing step is initiated. In the LIC-CB premixing case, a significantly lower amount of CB is collected by the LIC particles. It is evident that the addition of LFP results in a more pronounced increase in the fraction of collected CB aggregates, which approaches a comparable value at the end of the pipe as observed in the parallel mixing configuration. In the present simulation case, the maximum number of captured

LFP and LIC particles in free agglomerates is found at an axial particle distance of $2.94\ \mathrm{m}$. This is larger than the values found in the parallel and LFP-CB premixing simulations. At this stage, a significantly larger proportion of LIC has been deposited in comparison to the parallel mixing and LFP-CB premixing combination (see Fig. 13 a)). This is due to the fact that the LIC commences the process of agglomeration earlier, and the agglomerates that are formed subsequently exhibit increased deposition velocities. However, in this particular mixing combination, approximately 75% of the LIC particles are found within non-deposited agglomerates at this stage, with only 16% present as free-moving primary particles (see Fig. 13 b)).

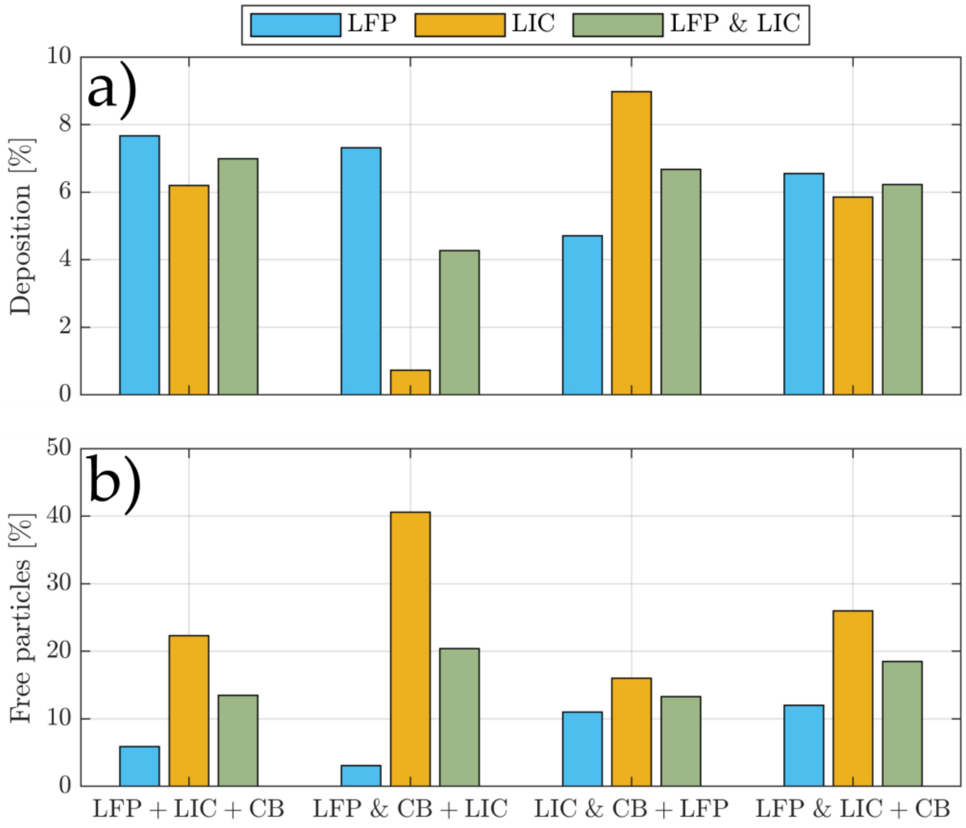

Fig. 13 a) Number fraction of deposited particles and b) number fraction of non-agglomerated and non-deposited particles for various mixing configurations at the respective axial particle distances, at which the maximum values of LFP and LIC particles captured in non-deposited agglomerates are observed.

The results of the LFP-LIC premixing simulation demonstrate that the relative agglomeration of LFP is very similar to that of LIC during premixing, as illustrated by the analogous graphs in Fig. 12. However, at the final stage of premixing, a slightly larger fraction of LIC particles has agglomerated, which can be attributed to the larger LIC-LIC collisions kernel (see Fig. 8 c)), caused by the wider particle size distribution of this material. When the CB is introduced as part of the subsequent mixing step, a strong discontinuity in the fraction of LFP and LIC being agglomerated is evident. As previously discussed, collisions involving LFP/LIC and CB are the most dominant, and the agglomeration rate therefore experiences an augmentation when CB is introduced. Once more, the effect of a larger LFP-CB than LIC-CB collision kernel is reflected by a larger slope of the graph showing the subsequent mixing LFP agglomeration when compared to that showing the LIC agglomeration. Since the carbon black has been introduced at a proceeded axial distance of approximately $1.74\ \mathrm{m}$, a significantly smaller fraction of CB has been agglomerated at the end of the pipe, where the maximum fraction of agglomerated LIC and LFP particles can also be found. At the stage of maximum agglomeration, it was found that only approximately 17% of carbon black is a constituent of non-deposited agglomerates containing LFP or LIC particles, while this value is approximately 30% in the case of LFP-CB premixing and approximately 27% in the case of LIC-CB premixing and parallel mixing.

Fig. 14 a) shows the mass-related particle/agglomerate size distribution (PSD) at the pipe position with the maximum LFP and LIC capture for all mixing configurations. It can be observed that, in all cases, the PSD is significantly shifted towards larger agglomerates when compared to the initial particle/aggregate size distribution indicated by the grey dashed line. In the range of medium agglomerate sizes ($1.5\ \mu\mathrm{m} < d < 10\ \mu\mathrm{m}$), the PSDs resulting from the different mixing configurations are very similar. However, the premixing of LFP with CB results in a modest shift towards larger agglomerates within this range, as evidenced by a marginally elevated mass-related median size (see Fig. 14 a)). In the range of large agglomerates ($10\ \mu\mathrm{m} < d < 50\ \mu\mathrm{m}$), disparities in size distribution can be observed between the various mixing configurations. The largest agglomerate is observed in the parallel mixing case, while the 90th percentile diameter is the highest in the case of premixing LIC with CB ($d_{90,3} = 27.53\ \mu\mathrm{m}$) and the smallest in the case of LFP-LIC premixing ($d_{90,3} = 16.69\ \mu\mathrm{m}$).

A more profound comprehension of the resulting agglomerate sizes is facilitated by an examination of the mass-weighted mean particle numbers within the agglomerates. This is due to the fact that these numbers also reflect the composition of the individual materials. These are demonstrated in Fig. 14 b) for each mixing configuration at the stage at which the maximum values of LFP and LIC particles captured in non-deposited agglomerates are observed. The mass-weighted number of CB aggregates in the agglomerates is almost identical when comparing parallel mixing and LIC-CB premixing, and is marginally lower in the case of LFP-CB premixing. This observation can be attributed to the faster deposition of LFP when compared to the deposition of LIC. In the case of LFP-CB premixing, large agglomerates containing already many CB aggregates are deposited more quickly. In the case of LFP-CB premixing, the heavy agglomerates consist predominantly of LFP, while in the parallel mixing configuration, the overrepresentation of LFP is smaller. In the case of LIC-CB premixing, heavy agglomerates contain a greater number of LIC agglomerates than LFP agglomerates. It can be hypothesized that large agglomerates formed from the LIC-CB premixing case are lighter than those formed from other mixing configurations. This phenomenon can be attributed to the reduced average diameter of LIC particles and their comparatively lower density. Consequently, reduced deposition of large particles results in elevated 90th percentile diameters in the case of LIC-CB premixing.

In the mixing configuration where LFP is premixed with LIC, a reduced mass-weighted mean number of particles/aggregates per agglomerate can be observed for all materials. As anticipated, the decrease in CB aggregate number is most pronounced. The reduced mean LFP and LIC numbers per agglomerate can be explained by the fact that the maximum number of agglomerated LFP and LIC particles would be reached for axial pipe distances greater than the pipe length itself. It is evident that the mass-weighted mean particle number per agglomerate would increase significantly if large agglomerates had more time to further agglomerate with one another. This phenomenon is further elucidated by the comparatively low 90th percentile diameter observed in the case of LFP-LIC premixing.

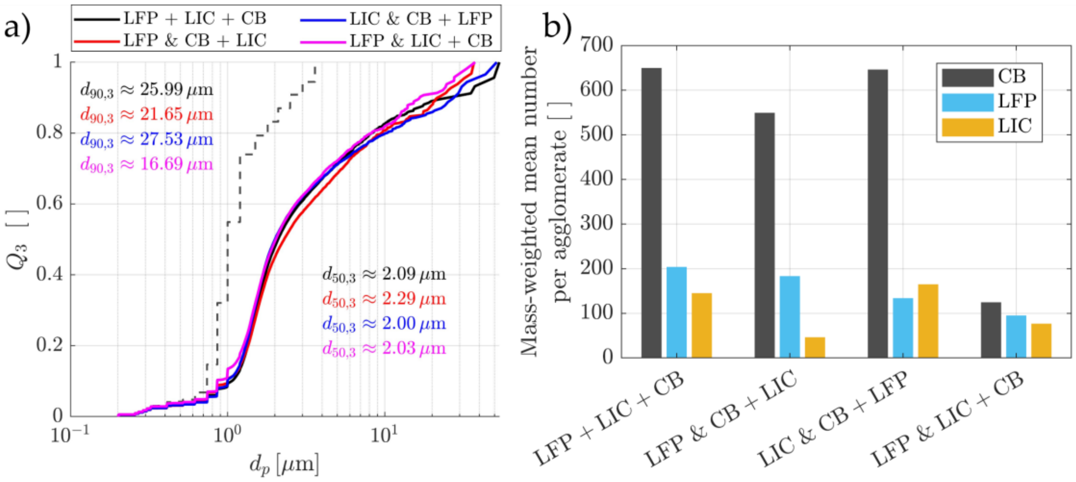

Fig. 14 a) Mass-related particle and agglomerate size distribution sum and b) mass-weighted mean CB aggregate and LFP/LIC particle number per agglomerate for different mixing configurations at the respective axial particle distances, at which the maximum values of LFP and LIC particles captured in non-deposited agglomerates are observed. For the purpose of comparison, the size distribution initial to the simulation is shown in a) as a grey dashed line. The respective mass-related median agglomerate/particle diameters $d_{50,3}$ and 90th percentile $d_{90,3}$ are shown for each mixing configuration in the respective colours.

4.4.2 Composition and mixing of hetero-agglomerates

The composition of the agglomerates formed under different mixing configurations is analysed by considering the degree of mixing. Following the procedure for evaluating the mixing quality of hetero-agglomerates presented in (Buchheiser et al., 2026), three quantities are considered individually before being combined into a single mixing quality measure: the inter-agglomerate mixing index; the intra-agglomerate mixing index; and the homogeneity of the latter. The inter-agglomerate mixing index describes the distribution of materials across all agglomerates, while the intra-agglomerate mixing index depicts the mixing quality within an agglomerate. The intra-agglomerate mixing index describes the mixing quality within an agglomerate. For instance, an agglomerate composed of all materials in a good fractioning but having only a few hetero-contacts due to local clustering of individual materials would lead to a small intra-agglomerate mixing index. The third quantity is the homogeneity of the intra-agglomerate mixing index. This increases when the intra-agglomerate mixing index only varies very little from agglomerate to agglomerate.

Here, the degree of mixing is quantified by the Lacey mixing index, evaluated separately for each material $k \in \{\mathrm{LFP}, \mathrm{LIC}, \mathrm{CB}\}$. For a given material k the general Lacey mixing index is defined as

$$M_k = \frac{\sigma_{0,k}^2 - \sigma_k^2}{\sigma_{0,k}^2 - \sigma_{\mathrm{r},k}^2}, \tag{28}$$

where

$$\sigma_{0,k}^2 = p_k(1 - p_k) \tag{29}$$

denotes the variance of a fully segregated state, and the possible minimum variance, which is set to zero in this work in order to compare the mixing to a reference state of perfect order, is denoted by $\sigma_{\mathrm{r},k}^2$. The quantity p_k denotes the relevant mean fraction of material k in the chosen sampling scheme and σ_k^2 is the observed variance for that scheme. In all evaluations, the mixing index is constrained to the interval $[0, 1]$ in order to avoid small numerical deviations outside the theoretical bounds.

For the inter-agglomerate index, each agglomerate a (total of N_A agglomerates) is treated as a sample. The local fraction of material k in agglomerate a is defined as

$$x_{a,k} = \frac{n_{a,k}}{n_{\mathrm{p},a}}, \tag{30}$$

where $n_{a,k}$ denotes the number of particles of material k in agglomerate a and $n_{\mathrm{p},a}$ denotes the number of counting units in that agglomerate (in the case of CB, the primary CB aggregate is counted as one single unit). The material fractions of all individual agglomerates are illustrated in Fig. 16 as a barycentric representation of the agglomerate composition, resulting from different mixing configurations, and will be discussed in more detail later. The overall fraction is computed as the particle-weighted mean

$$p_k = \frac{1}{N_\mathrm{P}} \sum_{a=1}^{N_\mathrm{A}} \left(n_{\mathrm{p},a}\, x_{a,k}\right) = \frac{1}{N_\mathrm{P}} \sum_{a=1}^{N_\mathrm{A}} \left(n_{a,k}\right), \tag{31}$$

where $N_\mathrm{P} = \sum_a n_{\mathrm{p},a}$ is the total number of particles/aggregates in all N_A agglomerates. The overall inter-agglomerate variance is evaluated as follows

$$\sigma_k^2 = \frac{1}{N_\mathrm{P}} \sum_{a=1}^{N_\mathrm{A}} n_{\mathrm{p},a} \left(x_{a,k} - p_k \right)^2 . \tag{32}$$

It should be noted that this formulation describes a number-weighted variance, thereby accounting for differences in agglomerate size. The inter-agglomerate Lacey index $M_k^{\mathrm{inter}} \in (0,1)$ is then obtained by inserting p_k and σ_k^2 into the general expression of the Lacey mixing Index (see Eq. (28)).

The intra-agglomerate mixing index quantifies the degree of mixing within an individual agglomerate a. To that end, each agglomerate is discretized by cubic cells that cover at least the entire volume occupied by an agglomerate. The cell size is selected to be two times the number-related 95th percentile diameter in the system ($ds_\mathrm{c} = 2 \times d_{95,0} = 2.4\ \mu\mathrm{m}$). It is imperative to acknowledge the necessity of maintaining a constant cell size in order to facilitate a meaningful comparison. Consequently, agglomerates with a radius of gyration that is less than the cell size are not taken into consideration. It is evident that the evaluation of the mixing quality of agglomerates of this size becomes invalid due to the presence of a minimal number of particles. For each cell i containing $n_{i,k}$ particles of material k and a total of $n_{\mathrm{p},i}$ particles, the cell's local material number fraction is given by:

$$x_{i,k} = \frac{n_{i,k}}{n_{\mathrm{p},i}} . \tag{33}$$

For each agglomerate a comprising $N_\mathrm{P}^{(a)}$ particles being discretized by $N_\mathrm{c}^{(a)}$ cells containing at least one particle, the mean and variance of the cells are computed as follows:

$$p_k^{(a)} = \frac{1}{N_\mathrm{P}^{(a)}} \sum_{i=1}^{N_\mathrm{c}^{(a)}} n_{\mathrm{p},i}\, x_{i,k} , \tag{34}$$

and

$$\sigma_k^{2(a)} = \frac{1}{N_\mathrm{P}^{(a)}} \sum_{i=1}^{N_\mathrm{c}^{(a)}} \left(x_{i,k} - p_k^{(a)} \right)^2 , \tag{35}$$

respectively. The intra-agglomerate Lacey index $M_k^{(a)}$ of an agglomerate a is obtained by inserting $p_k^{(a)}$ and $\sigma_k^{2(a)}$ into the general expression of the Lacey mixing Index (see Eq. (28)).

Following the determination of the individual intra-agglomerate mixing indices, a material dependent particle number-weighted mean index across agglomerates is formed as

$$\overline{M}_k = \frac{1}{\sum_{a=1}^{N_\mathrm{A}} N_{\mathrm{P},k}^{(a)}} \sum_{a=1}^{N_A} \left(N_{\mathrm{P},k}^{(a)} \, M_k^{(a)} \right), \tag{36}$$

where $N_{\mathrm{P},k}^{(a)}$ is the number of particles of material k in agglomerate a. The homogeneity of the intra-agglomerate mixing index is given by

$$\psi_{M_k} = 1 - \frac{\sigma_{M_k}^2}{\overline{M}_k \left(1 - \overline{M}_k\right)}, \tag{37}$$

where the particle number-weighted variance of the intra-agglomerate mixing index is

$$\sigma_{\mathrm{M}_k}^2 = \frac{1}{\sum_{a=1}^{N_a} N_{\mathrm{P},k}^{(a)}} \sum_{a=1}^{N_a} N_{P,k}^{(a)} \left(M_k^{(a)} - \overline{M}_k \right)^2. \tag{38}$$

As proposed by (Buchheiser et al., 2026), the overall mixing quality can be evaluated using a combined mixing quality measure

$$\psi_k^{\mathrm{comb}} = \frac{\delta \, \overline{M}_k + \varphi \psi_{M_k} + \omega M_k^{\mathrm{inter}}}{\delta + \varphi + \omega}. \tag{39}$$

In the present analysis, no weighting is conducted ($\delta = \varphi = \omega = 1$).

Fig. 15 shows all three mixing quality measures a) M_k^{inter}, b) $\overline{M}_k$ and c) ψ_{M_k} as well as the resulting combined mixing quality measure d) ψ_k^{comb} (uniform weighting) for all materials and different mixing configurations. Furthermore, the mean value of all materials is shown for each quality measure.

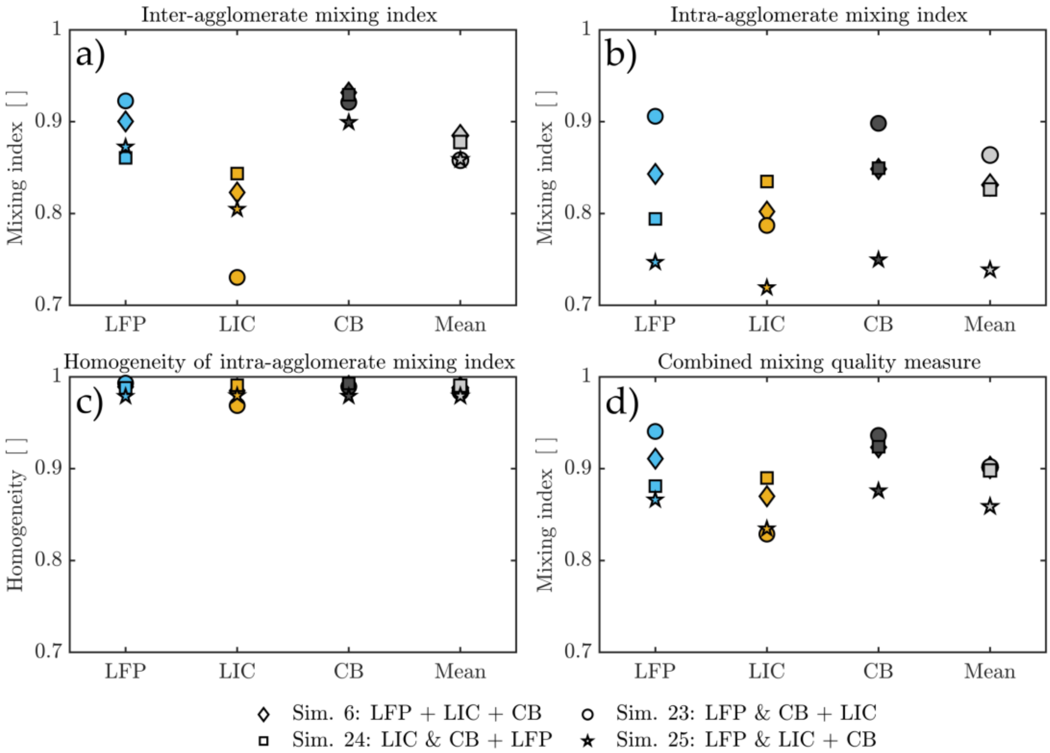

Fig. 15 a) Inter-agglomerate mixing index M_k^{inter}, b) mean intra-agglomerate Lacey mixing index $\overline{M}_k$, c) homogeneity of the intra-agglomerate mixing index ψ_{M_k} and d) combined mixing quality ψ_k^{comb} for all materials k and the resulting mean values. The results are shown for agglomerates at the axial pipe position at which the maximum values of LFP and LIC particles captured in non-deposited agglomerates are observed. The symbol "+" indicates parallel and sequential mixing, whereas "&" indicates premixing.

In all mixing configurations, the inter-agglomerate mixing index (see Fig. 15 a)) is shown to be lower for LIC than for LFP, which is attributable to the lower collision rates of LIC. As demonstrated in Fig. 13, in instances of parallel mixing, a proportion of LIC particles greater than 20% remain non-agglomerated at the stage in consideration. In the case of premixing LFP with CB, this value is even 40%. This finding aligns with the observations presented in Fig. 14 b), which demonstrate a lower mass-weighted mean number of LIC than LFP particles in the agglomerates for both configurations. Notably, the discrepancy is more pronounced in the case of LFP-CB premixing. This is also evident when considering the agglomerate composition in Fig. 16, where particularly the heavier agglomerates contain fewer LIC particles.

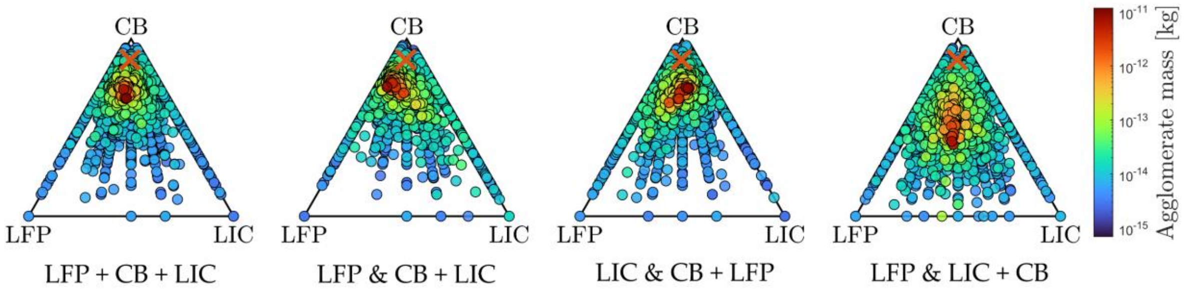

Fig. 16 Barycentric representation of the number-related agglomerate composition of LFP/LIC particles and CB aggregates ($x_{a,\mathrm{LFP}}$, $x_{a,\mathrm{LIC}}$ and $x_{a,\mathrm{CB}}$) for different mixing configurations coloured according to the respective mass of agglomerate a. The crosses indicate the number composition of the particles/aggregates in the seeding materials. The symbol "+" indicates parallel and sequential mixing, whereas "&" indicates premixing.

In terms of the mixing index, slower or later agglomeration of a material leads to poorer inter-agglomerate mixing (see Fig. 15 a)). This is because further agglomerate growth increases the number-weighted inter-agglomerate mixing index, provided a mixing state is reached at the flow level. To illustrate this, one might consider two separated pure homo-agglomerates containing all particles in the system. It can be posited that these would exhibit a mixing index of $M_1^{\mathrm{inter}} = 0$ and $M_2^{\mathrm{inter}} = 0$ prior to an agglomeration event (1+2 → 3) and a mixing index of $M_3^{\mathrm{inter}} = 1$ in the aftermath.

This observation is reinforced by the fact that in the case of parallel mixing, the difference between the LFP and LIC inter-agglomerate mixing index is smaller than for the LFP-CB premixing, where the agglomeration of LIC starts much later. Conversely, the premixing of LIC with CB results in a substantial augmentation of LIC and a reduction in the LFP inter-agglomerate mixing index (see Fig. 15 a)), thereby ensuring that both values approach equivalence in this configuration. In this instance, the heaviest agglomerates contain more LIC than LFP particles (see again Fig. 16). However, most of the large agglomerates have a comparatively equal number composition.

The inter-agglomerate mixing indices of all materials in the case of premixing LFP and LIC are smaller than those resulting from the parallel mixing configuration (see Fig. 15 a)). The poorer CB mixing index is due to the previously observed effect of a later onset of agglomeration, which in turn causes poorer inter-agglomerate mixing indices. The disparity in LFP and LIC mixing can be attributed to the higher number of LFP/LIC particles not being agglomerated with CB (see Fig. 13 b)), when compared to the parallel mixing configuration. The CB inter-agglomerate mixing index in the case of LIC-CB premixing is found to be almost identical to that resulting from parallel mixing. The value is marginally diminished in the instance of premixing LFP with CB, a phenomenon attributable to CB's propensity to agglomerate on LFP. This tendency is further substantiated by the initial exclusion of LIC-laden gas during the premixing process. Despite the fact that the individual materials exhibit different mixing indices, depending on the configuration under consideration, the mean values of the inter-agglomerate mixing index are identical when comparing parallel mixing with LIC-CB premixing and when comparing LFP-CB premixing with LFP-LIC premixing.

The <u>intra-agglomerate mixing index</u> demonstrates analogous trends (see Fig. 15 b)). The mixing index of LFP is higher than that of LIC (with the exception of premixing LIC with CB) and the mixing index of a specific material is increased by premixing it with CB. This phenomenon can be attributed to the predominance of CB-to-LFP or LIC contacts within the agglomerates, as illustrated in Fig. 17. The CB functions as a separator between the individual LFP or LIC particles, thereby increasing their intra-agglomerate mixing index. Nevertheless, it should be noted that inadequate mixing may also occur in the absence of homo-contacts, i.e., perfect separation of LFP or LIC particles by CB aggregates. This is applicable in instances where one material constitutes fragments of the agglomerate, and the other material comprises the remaining fragments, but all particles are separated by carbon black. However, in the case of LFP-CB premixing, the anticipated fraction of LIC per evaluation cell is considerably lower than in the other cases, which can be attributed to the reduced LIC particle number per agglomerate (see Fig. 14 b)). As a consequence, a considerable increase in the mixing index of LFP and CB is evident in this mixing configuration in comparison to the parallel mixing case. In contrast, a reduced mixing index of LIC can be observed. Similar, but opposite behaviour can be observed in the case of LIC being premixed with CB. Here, the intra-agglomerate mixing index of LIC is higher than that of LFP. One potential explanation for this phenomenon is the increased proportion of LIC within the agglomerates, as illustrated in Fig. 14 b)). Another related reason is the higher number of LIC-CB contacts. In the case of parallel mixing, $32.2\ \%$

of the detected contacts are between LIC and LFP. This number is reduced to $20.9\,\%$ in the case of LFP-CB premixing and increased to $41.5\,\%$ in the case of LIC-CB premixing (see Fig. 17). The mixing indices of all materials in the LFP-LIC premixing configuration are significantly lower and exhibit a comparable trend to the parallel mixing case, which can be attributed to the lower CB content. It is noteworthy that in this configuration, 10.2% of contacts are LFP-LIC, whereas LFP/LIC homo-contacts account for a mere 9.8% of contacts. This ratio is higher than in every other mixing configuration. The mean intra-agglomerate mixing index in the case of LIC-CB premixing is only marginally smaller than that resulting from parallel mixing. In contrast, the corresponding value is larger in the case of LFP-CB premixing, which is attributable to the increased CB intra-agglomerate mixing index.

The number-weighted homogeneity of the intra-agglomerate mixing index is greater than 0.95 for each material in each mixing configuration (see Fig. 15 c)). This finding suggests that the individual agglomerates possess mixing qualities that are highly similar. The disparities in the values obtained from the various mixing configurations are negligible for each material, and the mean values derived from these configurations are almost identical. Consequently, the homogeneity appears to augment the combined mixing quality measure of all materials in all configurations, without significantly influencing the differentiation between them. It is therefore evident that the combined mixing quality measure (see Fig. 15 d)) demonstrates a similar pattern to the inter- and intra-agglomerate mixing index. While the disparities in mixing quality between the LFP and the LIC are at their most pronounced in the case of LFP-CB premixing, these disparities are least pronounced in the case of premixing of LIC and CB. It is a noteworthy observation that, despite the evident disparities, the mean mixing quality is equivalent for the parallel mixing, LFP-CB premixing and LIC-CB premixing configurations.

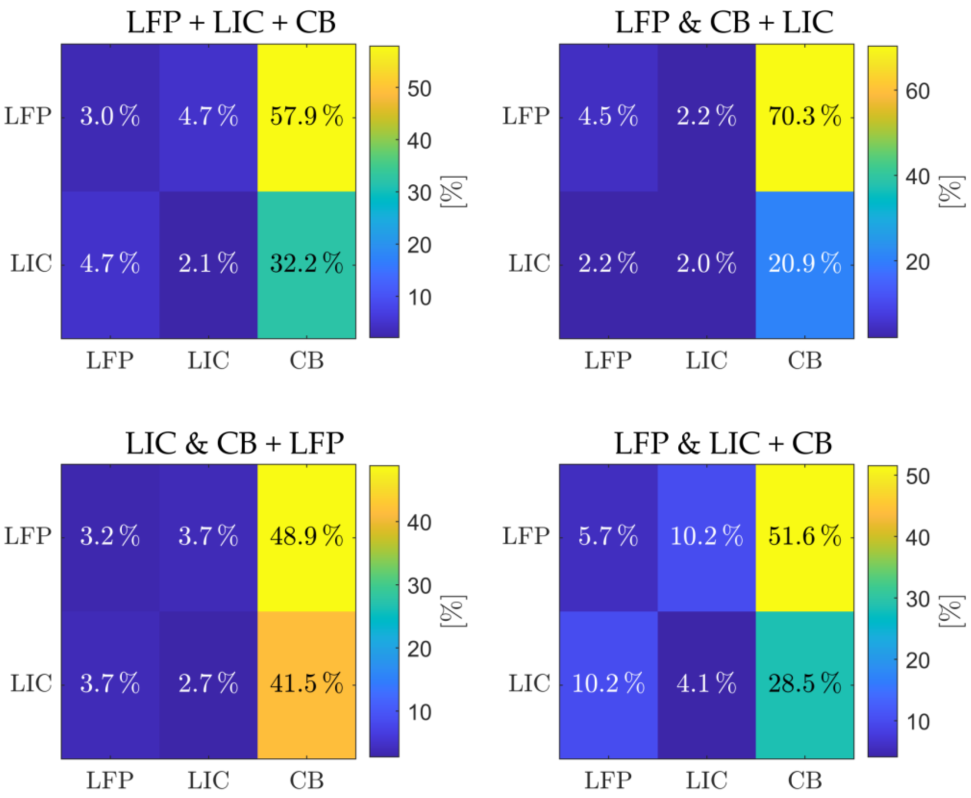

Fig. 17 Contact matrix showing the contact fractions of LFP and LIC with any other material type in different mixing configurations. The results are shown for agglomerates at the axial pipe position at which the maximum values of LFP and LIC particles captured in non-deposited agglomerates are observed. The symbol "+" indicates parallel and sequential mixing, whereas "&" indicates premixing.

However, the current state of knowledge does not yet allow for a definitive conclusion as to which mixing quantity of which material exerts the greatest influence on the electric and ionic conductivity of the formed material and the resulting capacity of the cell. It can be hypothesized that either the intra- or the inter-agglomerate mixing index holds greater significance than the other, i.e., $\delta \neq \varphi$. Furthermore, good mixing of one of the materials could be more important for the resulting electrochemical properties than good mixing of the other material. It is also conceivable that it would be beneficial if the mixing quality of all materials exhibited similar values, which could be quantified by introducing another homogeneity index similar to that presented in Eq. (37). Future work could identify the influence of different mixing quantities by simulating the electrical and ionic conductivity of numerically formed agglomerates or representative matrices, using either a resistor-network approach (Roussel et al., 2015; Sangrós Giménez et al., 2025) or a voxel-based approach (Laue et al., 2020; Roussel et al., 2015). Moreover, the influence of differences in the contact matrices illustrated in Fig. 17 could be identified therein. For instance, an increased number of LIC-LIC homo-contacts in the case of LIC-CB premixing (see Fig. 17) must not necessarily be associated with worse electrochemical properties, as continuous ion transport pathways are desirable and require LIC-LIC homo-contacts (Alsaç et al., 2025). This could also be an indication that a higher LFP mixing index and a smaller LIC mixing index are favourable. However, this must be numerically evaluated in future work. A further method of estimating the resulting electrochemical performance is to examine CAM utilization, which describes the proportion of the active material (LFP) that is in contact with at least one electrolyte particle (LIC) and one CB particle (Kissel et al., 2026b). The analysis of all three-component agglomerates indicates that the parallel mixture results in a CAM utilization of 36%. The values for the premixing of LFP with CB, LIC with CB, and LFP with LIC are 18%, 31%, and 38%, respectively. From this standpoint, the LFP-LIC premixing scenario appears to be the most promising. However, all values are comparatively low, which is due to the absence of LFP-LIC contacts rather than the absence of LFP-CB contacts. Within the present agglomerates, the LFP and LIC contacts are often separated by CB aggregates. Consequently, it is imperative to undertake a compaction or calendaring step prior to conducting a meaningful evaluation of CAM utilisation.

It is evident that the electrochemical performance of the composite is not solely dependent on its inherent structure, but is also contingent on the mass composition of all materials. However, it should be noted that the mass fractions of the materials within the formed hetero-agglomerates may differ from that resulting from the particle feed. Fig. 18 illustrates the normalized overall mass fractions of all materials, relative to their respective ideal (feed) mass fractions, for all configurations. Note that only three-component hetero-agglomerates are considered here. The parallel mixing case and the premixing of LFP with CB result in mass compositions that are very similar, with LFP being approximately at the desired value and LIC being slightly overrepresented. It is evident that CB is significantly underrepresented in all cases, particularly in the case of premixing LFP with LIC. This aligns with the poor CB-capturing observed in Fig. 12 c). This finding indicates that a substantially higher CB mass flow may be advantageous in the context of hetero-agglomerates being sampled separately from single CB aggregates. In the case of premixing LIC with CB and LFP with LIC, the deviation of the LFP and LIC mass fractions to the ideal value is greater than in the other instances. This phenomenon can be primarily explained by the high number of LFP-CB agglomerates not being part of three-component hetero-agglomerates. Moreover, it is imperative to acknowledge that in the context of optimal composition (LFP & CB + LIC), approximately 40% of the LIC particles remain non-agglomerated at this stage. Consequently, it is only appropriate to draw conclusions from this consideration for a practical application when hetero-agglomerates are separated from primary particles and CB-aggregates, for example by adding an electrostatic separation process downstream. As previously stated, it is recommended that CB feeding be augmented in such cases.

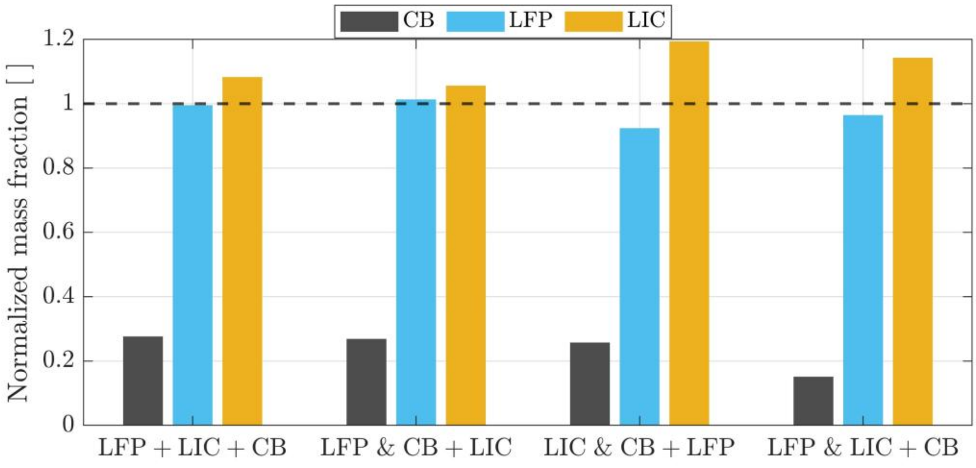

Fig. 18 Overall CB, LFP and LIC mass fractions in all agglomerates containing all materials normalized by the ideal mass ratio resulting from the mass flow (see Table 2). The results are shown for all mixing configurations at the respective axial particle distances, at which the maximum values of LFP and LIC particles captured in non-deposited agglomerates are observed. The dashed line indicates the unit value, which is achieved in the case of attaining the desired feed mass ratio. The symbol "+" indicates parallel and sequential mixing, whereas "&" indicates premixing.

5. Conclusions

The present study has analysed the mixing and hetero-agglomeration of LFP, LIC and CB in turbulent pipe flows. The aim of this analysis was to identify suitable pipe dimensions for the given process conditions and to evaluate the differences in agglomerate size, composition and structure that arise from different mixing configurations (parallel mixing and premixing of LFP with CB, LIC with CB and LFP with LIC). This objective was realized through the performance of four distinct simulation sets, incorporating Lagrangian agglomerate structure simulations.

In the initial set, the various collision mechanisms between the materials under investigation were evaluated for uniformly distributed particles in different pipes ($D_{\mathrm{pipe}} = 9$ and $12\ \mathrm{mm}$). It has been demonstrated that the accumulation effect is pronounced at a pipe diameter of $9\ \mathrm{mm}$ and its significance diminishes with an increase in pipe diameter. Considering collision efficiency proved to be imperative for collisions involving LFP and CB, as well as LIC and CB, because it significantly reduces their collision kernel. However, particularly for larger pipe diameters, it was shown that the resulting collision frequency of these collision partners is much higher than that of other combinations of materials.

The second simulation set aimed to model the hetero-agglomeration in the parallel mixing configurations in pipes of various diameters ($D_{\mathrm{pipe}} = 9, 12, 15, 18$ and $21\ \mathrm{mm}$) with a fixed pipe length of $L_{\mathrm{pipe}} = 3.5\ \mathrm{m}$. It was found that an $18\ \mathrm{mm}$ pipe diameter is suitable for the given process conditions (i.e., gas volume flow, particle mass flows and particle size distributions) in the case of parallel mixing. However, larger pipe diameters might also be suitable when experimental implementation allows for larger pipe lengths, since the hetero-agglomeration process necessitates longer axial distances to result in comparable agglomerate sizes in such instances. The pipe diameter that has been selected allows for a high proportion of primary particles to be captured in agglomerates, with a maximum at $x_{\mathrm{pipe}} = 2.73\ \mathrm{m}$. This results in a satisfactory ratio of hetero-contacts to homo-contacts, as well as the formation of large agglomerates. Should pipe diameters be smaller, greater deposition will be observed, thus requiring shorter pipe lengths to avoid mass loss.

In the third simulation set, a pipe diameter variation was conducted in the simulation framework with the objective of identifying a suitable pipe diameter for the premixing process in every combination (LFP with CB, LIC with CB and LFP with LIC). The simulations were terminated when a state of mixing, defined as the Lacey index being greater than 0.98, was reached. The objective of this simulation set was to ascertain the pipe diameter that would yield the shortest axial mixing distance, while also minimizing deposition. Premixing LFP with CB was found to be optimal with a pipe diameter of $D_{\text{pipe}} = 12\ \text{mm}$, resulting in a mixing length of $0.63\ \text{m}$. Sufficient mixing of LIC with CB was achieved at an axial pipe position of $0.65\ \text{m}$ with a pipe diameter of $D_{\text{pipe}} = 15\ \text{mm}$. For premixing LFP with LIC, the optimum pipe diameter was found to be $D_{\text{pipe}} = 21\ \text{mm}$, resulting in a mixing length of $1.72\ \text{m}$.

The particle and agglomerate data resulting from the premixing simulations have been utilized in the respective simulations of the subsequent mixing step, where the pipe diameter was fixed at $18\ \text{mm}$, allowing for a comparison with the parallel mixing configuration. The subsequent mixing step was initiated at the pipe distance at which the respective premixing simulation was terminated and terminated at a fixed pipe length of $L_{\text{pipe}} = 3.5\ \text{m}$. The maximum fraction of captured LFP and LIC particles was found at a pipe length of $x_{\text{pipe}} = 2.45\ \text{m}$ in the case of LFP-CB premixing, at a pipe length of $x_{\text{pipe}} = 2.94\ \text{m}$ in the case of LIC-CB premixing, and at the pipe termination $(x_{\text{pipe}} = L_{\text{pipe}} = 3.5\ \text{m})$ in the case of LFP-LIC premixing. The latter suggests that increased pipe length may be advantageous in achieving the desired outcomes of this configuration. The simulations revealed that the configuration of LFP-LIC premixing resulted in smaller agglomerates, an inadequate CB content, and inferior mixing quality when compared to the other configurations. The findings of this simulation set demonstrate that the agglomerate composition, particularly that of the large agglomerates, is significantly influenced by different mixing configurations.

The configurations of parallel mixing and premixing LIC with carbon black both result in larger agglomerates (see Fig. 14 a) and b)) and fewer unbounded primary particles (see Fig. 13 b)) when compared to the other configurations. However, the slower agglomerate growth in the case of premixing LFP with CB leads to less deposition (see Fig. 13 a)) in this case. The parallel mixing configuration, as well as the LFP-CB premixing, both result in a similar mass composition within three-component hetero-agglomerates, which is superior to that observed in the case of LIC-CB premixing. In all cases, the mass fraction of CB is found to be significantly lower than the desired value. In potential future processes where large agglomerates are separated from the CB aggregates, this issue should be addressed by increasing the CB mass flow rate. From the perspective of these quantities, the parallel mixing configuration is recommended, as it leads to both the formation of larger agglomerates and a satisfactory mass composition, at least with respect to LIC and LFP particles.

However, with regard to the objective of achieving optimal electrochemical performance, other variables, including the number of various contact combinations and the mixing index, may also be instrumental in determining the selection of an appropriate mixing configuration. The diverse mixing configurations exhibited a significant impact on the contact matrices of the three materials, in addition to their inter- and intra-agglomerate mixing quality. A comparison to the parallel mixing configuration reveals that premixing of LFP results in elevated LFP mixing indices and diminished LIC mixing indices. Conversely, the premixing of LIC results in more homogeneous mixing indices for the various materials. The mean value of the combined mixing quality measure demonstrated uniformity across all materials, with the exception of the agglomerates resulting from LFP-LIC premixing, which exhibited a reduced quality. An increased number of LIC-LIC contacts in the case of LIC-CB premixing (see Fig. 17) in combination with a good mixing performance could indicate, for example, that this configuration is advantageous in terms of ionic conductivity. In future work, a correlation between the various mixing indices and the resulting electrochemical properties of the composite, utilizing, for instance, resistor-network simulations, could be established in order to identify hetero-agglomerate structures (resulting from different mixing configurations) showing good electrochemical performance.

Declaration of Competing Interest

The authors declare that they have no known competing financial interests or personal relationships that could have appeared to influence the work reported in this paper.

Acknowledgment

The Priority Programme (SPP 2289) is funded by the Deutsche Forschungsgemeinschaft (DFG, German Research Foundation) – Project-IDs: 462460600, 462470125 and 462365306. Computing resources were partly funded by the DFG – Project-ID: 463921749.

References

Alsaç, E.P., Nelson, D.L., Yoon, S.G., Cavallaro, K.A., Wang, C., Sandoval, S.E., Eze, U.D., Jeong, W.J., McDowell, M.T., 2025. Characterizing Electrode Materials and Interfaces in Solid-State Batteries. Chem. Rev. 125, 2009–2119. https://doi.org/10.1021/acs.chemrev.4c00584

Buades, A., Coll, B., Morel, J.-M., 2005. A Non-Local Algorithm for Image Denoising, in: 2005 IEEE Computer Society Conference on Computer Vision and Pattern Recognition (CVPR’05). IEEE, pp. 60–65. https://doi.org/10.1109/CVPR.2005.38

Buchheiser, S., Furat, O., Schmidt, V., Nirschl, H., Rhein, F., 2026. Assessing the Mixing Quality of Hetero-Aggregates: Applying Mixing Theory to STEM-EDX Elemental Maps. Particle & Particle Systems Characterization 43, e00172. https://doi.org/10.1002/ppsc.202500172

Buchheiser, S., Kistner, F., Rhein, F., Nirschl, H., 2023. Spray Flame Synthesis and Multiscale Characterization of Carbon Black–Silica Hetero-Aggregates. Nanomaterials 13, 1893. https://doi.org/10.3390/nano13121893

Caporaloni, M., Tampieri, F., Trombetti, F., Vittori, O., 1975. Transfer of Particles in Nonisotropic Air Turbulence. J. Atmos. Sci. 32, 565–568. https://doi.org/10.1175/1520-0469(1975)032<0565:TOPINA>2.0.CO;2

Cheng, Z., Zahiri, B., Ji, X., Chen, C., Chalise, D., Braun, P. V., Cahill, D.G., 2021. Good Solid-State Electrolytes Have Low, Glass-Like Thermal Conductivity. Small 17, 2101693. https://doi.org/10.1002/smll.202101693

Cunningham, E., 1910. On the velocity of steady fall of spherical particles through fluid medium. Proceedings of the Royal Society of London. Series A, Containing Papers of a Mathematical and Physical Character 83, 357–365. https://doi.org/10.1098/rspa.1910.0024

Dominik, C., Tielens, A.G.G.M., 1997. The physics of dust coagulation and the structure of dust aggregates in space. Astrophys. J. 480, 647–673. https://doi.org/10.1086/303996

El Khoury, G.K., Schlatter, P., Noorani, A., Fischer, P.F., Brethouwer, G., Johansson, A. V., 2013. Direct Numerical Simulation of Turbulent Pipe Flow at Moderately High Reynolds Numbers. Flow Turbul. Combust. 91, 475–495. https://doi.org/10.1007/s10494-013-9482-8

Filippov, A.V., Zurita, M., Rosner, D.E., 2000. Fractal-like Aggregates: Relation between Morphology and Physical Properties. J. Colloid Interface Sci. 229, 261–273. https://doi.org/10.1006/jcis.2000.7027

Frankenberg, F., Heck, C.A., Kissel, M., Lange, M.A., Faka, V., Diener, A., Haase, P., Michalowski, P., Zeier, W.G., Janek, J., Kwade, A., 2025. Tailoring Composite Microstructure Through Milling for Dry-Processed Sulfide-Based Solid-State Battery Cathodes. Small 21. https://doi.org/10.1002/smll.202507279

Frankenberg, F., Kissel, M., Burmeister, C.F., Lippke, M., Janek, J., Kwade, A., 2024. Investigating the production of all-solid-state battery composite cathodes by numerical simulation of the stressing conditions in a high-intensity mixer. Powder Technol. 435, 119403. https://doi.org/10.1016/j.powtec.2024.119403

Fuchs, L., Furat, O., Finegan, D.P., Allen, J., Usseglio-Viretta, F.L.E., Ozdogru, B., Weddle, P.J., Smith, K., Schmidt, V., 2025a. Generating multi-scale Li-ion battery cathode particles with radial grain architectures using stereological generative adversarial networks. Commun. Mater. 6, 4. https://doi.org/10.1038/s43246-024-00728-5

Fuchs, L., Kirstein, T., Mahr, C., Furat, O., Baric, V., Rosenauer, A., Mädler, L., Schmidt, V., 2024. Using convolutional neural networks for stereological characterization of 3D hetero-aggregates based on synthetic STEM data. Mach. Learn. Sci. Technol. 5, 025007. https://doi.org/10.1088/2632-2153/ad38fd

Fuchs, L., Wein, K., Friedland, J., Furat, O., Güttel, R., Schmidt, V., 2025b. Stereological 3D modeling of nano-scale catalyst particles using TEM projections. Mach. Learn. Sci. Technol. 6, 035014. https://doi.org/10.1088/2632-2153/ade92d

Gerken, B., Mahr, C., Stahl, J., Grieb, T., Schowalter, M., Krause, F.F., Mehrtens, T., Mädler, L., Rosenauer, A., 2023. Material Discrimination in Nanoparticle Hetero-Aggregates by Analysis of Scanning Transmission Electron Microscopy Images. Particle & Particle Systems Characterization 40, 2300048. https://doi.org/10.1002/ppsc.202300048

Gosman, A.D., Ioannides, E., 1983. Aspects of Computer Simulation of Liquid-Fueled Combustors. Journal of energy 7, 482–490. https://doi.org/10.2514/3.62687

Gunlazuardi, J., Fisli, A., Ridwan, R., Krisnandi, Y.K., Robert, D., 2021. Magnetically Separable Fe3O4/SiO2/TiO2 Photocatalyst Composites Prepared through Hetero Agglomeration for the Photocatalytic Degradation of Paraquat. Makara J. Sci. 25. https://doi.org/10.7454/mss.v25i4.1277

Hornbogen, E., Eggeler, G., Werner, E., 2019. Werkstoffe. Springer Vieweg, Berlin. https://doi.org/10.1007/978-3-662-58847-5

Janek, J., Zeier, W.G., 2016. A solid future for battery development. Nat. Energy 1, 16141. https://doi.org/10.1038/nenergy.2016.141

Jean, A., Willot, F., Cantournet, S., Forest, S., Jeulin, D., 2011. Large-scale computations of effective elastic properties of rubber with carbon black fillers. Int. J. Multiscale Comput. Eng. 9, 271–303. https://doi.org/10.1615/IntJMultCompEng.v9.i3.30

Jeong, J., Lee, H., Choi, J., Ryou, M.-H., Lee, Y.M., 2015. Effect of LiFePO4 cathode density and thickness on electrochemical performance of lithium metal polymer batteries prepared by in situ thermal polymerization. Electrochim. Acta 154, 149–156. https://doi.org/10.1016/j.electacta.2014.12.051

Jin, X., Shen, Y., 2024. Current Progress of Experimental and Simulation Work of Mixing Processes in Particulate Systems. KONA Powder and Particle Journal 41, 2024015. https://doi.org/10.14356/kona.2024015

Jung, Y.S., Oh, D.Y., Nam, Y.J., Park, K.H., 2015. Issues and Challenges for Bulk-Type All-Solid-State Rechargeable Lithium Batteries using Sulfide Solid Electrolytes. Isr. J. Chem. 55, 472–485. https://doi.org/10.1002/ijch.201400112

Kaelble, D.H., 1970. Dispersion-Polar Surface Tension Properties of Organic Solids. J. Adhes. 2, 66–81. https://doi.org/10.1080/0021846708544582

Kerman, K., Luntz, A., Viswanathan, V., Chiang, Y.-M., Chen, Z., 2017. Review—Practical Challenges Hindering the Development of Solid State Li Ion Batteries. J. Electrochem. Soc. 164, A1731–A1744. https://doi.org/10.1149/2.1571707jes

Kissel, M., Frankenberg, F., Demuth, T., Lai, A., Laser, N., Wagner, D., Eisa, A., Michalowski, P., Volz, K., Kwade, A., Janek, J., 2026. Mechanofusion-derived cathode composite microstructures with scalable mixed conducting matrix coatings for solid state batteries. Nat. Commun. 17, 3215. https://doi.org/10.1038/s41467-026-71305-2

Kolck, V., Witte, J., Schmidt, E., Kruggel-Emden, H., 2026. Lagrangian modelling of direct mixing gas phase hetero-agglomeration in turbulent pipe flows. International Journal of Multiphase Flow 194, 105458. https://doi.org/10.1016/j.ijmultiphaseflow.2025.105458

Kolck, V., Witte, J., Schmidt, E., Kruggel-Emden, H., 2023a. Analysis of process parameter sensitivities of jet-based direct mixing gas phase hetero-agglomeration by DEM/CFD-modelling. Powder Technol. 429, 118963. https://doi.org/10.1016/j.powtec.2023.118963

Kolck, V., Witte, J., Schmidt, E., Kruggel-Emden, H., 2023b. DEM/CFD modelling of jet-based mixing gas phase hetero-agglomeration for the analysis of process parameter sensitivities, in: International Congress on Particle Technology 2023. Nürnberg, Germany, pp. 346–350.

Kolmogorov, A.N., 1991. The local structure of turbulence in incompressible viscous fluid for very large Reynolds numbers. Proc. R. Soc. Lond. A Math. Phys. Sci. 434, 9–13. https://doi.org/10.1098/rspa.1991.0075

Kruis, F.E., Kusters, K.A., 1997. The collision rate of particles in turbulent flow. Chem. Eng. Commun. 158, 201–230. https://doi.org/10.1080/00986449708936589

Kühn, N., Frankenberg, F., Kwade, A., Schilde, C., 2025. Determination of interaction forces of (sub)-micron sized particles via the capillary rise method and colloidal probe atomic force microscopy: A combined approach. J. Colloid Interface Sci. 680, 696–713. https://doi.org/10.1016/j.jcis.2024.10.187

Lacey, P.M.C., 1954. Developments in the theory of particle mixing. Journal of Applied Chemistry 4, 257–268. https://doi.org/10.1002/jctb.5010040504

Laue, V., Wolff, N., Röder, F., Krewer, U., 2020. Modeling the Influence of Mixing Strategies on Microstructural Properties of All-Solid-State Electrodes. Energy Technology 8, 1801049. https://doi.org/10.1002/ente.201801049

Li, A., Ahmadi, G., 1993. Deposition of aerosols on surfaces in a turbulent channel flow. Int. J. Eng. Sci. 31, 435–451. https://doi.org/10.1016/0020-7225(93)90017-O

Li, Q., Yu, H., Li, K., Yin, H., Zhou, S., 2019. Controlled Synthesis and Enhanced Catalytic Activity of Well-Defined Close-Contact Pd–ZnO Nanostructures. Langmuir 35, 6288–6296. https://doi.org/10.1021/acs.langmuir.9b00252

Liu, X., Wang, K., Tan, X., Zeng, H., Liu, Q., 2022. Removal of fine solids from bitumen by hetero-aggregation and magnetic separation using surface-modified magnetite nanoparticles. Part 1: Proof of concept. Sep. Purif. Technol. 300, 121840. https://doi.org/10.1016/j.seppur.2022.121840

Li, X., Liang, J., Chen, N., Luo, J., Adair, K.R., Wang, C., Banis, M.N., Sham, T., Zhang, L., Zhao, S., Lu, S., Huang, H., Li, R., Sun, X., 2019. Water-Mediated Synthesis of a Superionic Halide Solid Electrolyte. Angewandte Chemie 131, 16579–16584. https://doi.org/10.1002/ange.201909805

Lucas, R., 1918. Ueber das Zeitgesetz des kapillaren Aufstiegs von Flüssigkeiten. Kolloid-Zeitschrift 23, 15–22. https://doi.org/10.1007/BF01461107

Mandelbrot, B.B., 1982. The Fractal Geometry of Nature. W.H. Freeman and Company, New York.

Maxisch, T., Ceder, G., 2006. Elastic properties of olivine LixFePO4 from first principles. Phys. Rev. B 73, 174112. https://doi.org/10.1103/PhysRevB.73.174112

Mclaughlin, J.B., 1993. The lift on a small sphere in wall-bounded linear shear flows. J. Fluid Mech 246, 249–265. https://doi.org/10.1017/S0022112093000114

Mei, R., 1992. An approximate expression for the shear lift force on a spherical particle at finite reynolds number. International Journal of Multiphase Flow 18, 145–147. https://doi.org/10.1016/0301-9322(92)90012-6

Mofakham, A.A., Ahmadi, G., 2020. Improved discrete random walk stochastic model for simulating particle dispersion and deposition in inhomogeneous turbulent flows. Journal of Fluids Engineering, Transactions of the ASME 142. https://doi.org/10.1115/1.4047538

Molaiyan, P., Mailhiot, S.E., Voges, K., Kantola, A.M., Hu, T., Michalowski, P., Kwade, A., Telkki, V.-V., Lassi, U., 2023. Investigation of the structure and ionic conductivity of a Li3InCl6 modified by dry room annealing for solid-state Li-ion battery applications. Mater. Des. 227, 111690. https://doi.org/10.1016/j.matdes.2023.111690

Mościński, J., Bargieł, M., Rycerz, Z.A., Jacobs, P.W.M., 1989. The Force-Biased Algorithm for the Irregular Close Packing of Equal Hard Spheres. Mol. Simul. 3, 201–212. https://doi.org/10.1080/08927028908031373

Otsu, N., 1979. A Threshold Selection Method from Gray-Level Histograms. IEEE Trans. Syst. Man Cybern. 9, 62–66. https://doi.org/10.1109/TSMC.1979.4310076

Owens, D.K., Wendt, R.C., 1969. Estimation of the surface free energy of polymers. J. Appl. Polym. Sci. 13, 1741–1747. https://doi.org/10.1002/app.1969.070130815

Parker, S.C., Kerisit, S., Marmier, A., Grigoleit, S., Watson, G.W., 2003. Modelling inorganic solids and their interfaces: A combined approach of atomistic and electronic structure simulation techniques. Faraday Discuss. 124, 155–170. https://doi.org/10.1039/b211988a

Poux, M., Fayolle, P., Bertrand, J., Bridoux, D., Bousquet, J., 1991. Powder mixing: Some practical rules applied to agitated systems. Powder Technol. 68, 213–234. https://doi.org/10.1016/0032-5910(91)80047-M

Rabel, W., 1971. Einige Aspekte der Benetzungstheorie und ihre Anwendung auf die Untersuchung und Veränderung der Oberflächeneigenschaften von Polymeren. Farbe und Lack 77, 997–1005.

Reeks, M.W., 1983. The transport of discrete particles in inhomogeneous turbulence. J. Aerosol Sci. 14, 729–739. https://doi.org/10.1016/0021-8502(83)90055-1

Ripley, B.D., 1987. Stochastic Simulation. Wiley. https://doi.org/10.1002/9780470316726

Roussel, D., Lichtner, A., Jauffrès, D., Bordia, R.K., Martin, C.L., 2015. Effective transport properties of 3D multi-component microstructures with interface resistance. Comput. Mater. Sci. 96, 277–273. https://doi.org/10.1016/j.commatsci.2014.09.027

Russ, J.C., 2006. The Image Processing Handbook, 5th ed. CRC Press.

Saffman, P.G., 1968. The lift on a small sphere in a slow shear flow - Corrigendum. J. Fluid Mech. 31, 624–624. https://doi.org/10.1017/S0022112068999990

Saffman, P.G., 1965. The lift on a small sphere in a slow shear flow. J. Fluid Mech. 22, 385–400. https://doi.org/10.1017/S0022112065000824

Sangrós Giménez, C., Helmers, L., Schilde, C., Diener, A., Kwade, A., 2020. Modeling the Electrical Conductive Paths within All-Solid-State Battery Electrodes. Chem. Eng. Technol. 43, 819–829. https://doi.org/10.1002/ceat.201900501

Sangrós Giménez, C., Pistoor, A., Willuhn, C., Schilde, C., Kwade, A., 2025. Modelling the electrical conductivity of Lithium-ion battery electrodes via a bonded-particle approach. Advanced Powder Technology 36, 104931. https://doi.org/10.1016/j.apt.2025.104931

Schiller, L., Naumann, A., 1933. Über die grundlegende Berechnungen bei der Schwerkraftaufbereitung. Zeitschrift des Vereines deutscher Ingenieure 12, 318–320.

Schneider, R., 2013. Convex Bodies: The Brunn-Minkowski Theory. Cambridge University Press. https://doi.org/10.1017/CBO9781139003858

Schnell, J., Günther, T., Knoche, T., Vieider, C., Köhler, L., Just, A., Keller, M., Passerini, S., Reinhart, G., 2018. All-solid-state lithium-ion and lithium metal batteries – paving the way to large-scale production. J. Power Sources 382, 160–175. https://doi.org/10.1016/j.jpowsour.2018.02.062

Schuch, G., Löffler, F., 1978. Über die Abscheidewahrscheinlichkeit von Feststoffpartikeln an Tropfen in einer Gasströmung durch Trägheitseffekte, in: Verfahrenstechnik. pp. 302–306.

Sedlatschek, T., Krämer, M., Gibson, J.S.K.-L., Korte-Kerzel, S., Bezold, A., Broeckmann, C., 2022. Mechanical properties of heterogeneous, porous LiFePO4 cathodes obtained using statistical nanoindentation and micromechanical simulations. J. Power Sources 539, 231565. https://doi.org/10.1016/j.jpowsour.2022.231565

Sippola, M.R., Nazaroff, W.W., 2002. Particle deposition from turbulent flow: Review of published research and its applicability to ventilation ducts in commercial buildings. Lawrence Berkeley National Laboratory Report LBNL – 51432. https://doi.org/10.2172/815478

Slinn, W.G.N., 1977. Some approximations for the wet and dry removal of particles and gases from the atmosphere. Water Air Soil Pollut. 7. https://doi.org/10.1007/BF00285550

Sommerfeld, M., 2001. Validation of a stochastic Lagrangian modelling approach for inter-particle collisions in homogeneous isotropic turbulence. International Journal of Multiphase Flow 27, 1829–1858. https://doi.org/10.1016/S0301-9322(01)00035-0

Sommerfeld, M., Stübing, S., 2017. A novel Lagrangian agglomerate structure model. Powder Technol. 319, 34–52. https://doi.org/10.1016/j.powtec.2017.06.016

Sorensen, C.M., 2011. The Mobility of Fractal Aggregates: A Review. Aerosol Science and Technology 45, 765–779. https://doi.org/10.1080/02786826.2011.560909

Spahr, M.E., Goers, D., Leone, A., Stallone, S., Grivei, E., 2011. Development of carbon conductive additives for advanced lithium ion batteries. J. Power Sources 196, 3404–3413. https://doi.org/10.1016/j.jpowsour.2010.07.002

Stanley, H.E., Ostrowsky, N., 1985. On Growth and Form. Springer Netherlands, Dordrecht. https://doi.org/10.1007/978-94-009-5165-5

Wang, G., Chen, L., Mathur, G.N., Varadan, V.K., 2012. Lithium iron phosphates as cathode materials in lithium ion batteries for electric vehicles, in: Proceedings of SPIE - The International Society for Optical Engineering. p. 83440L. https://doi.org/10.1117/12.915638

Wang, L.-P., Wexler, A.S., Zhou, Y., 2000. Statistical mechanical description and modelling of turbulent collision of inertial particles. J. Fluid Mech. 415, 117–153. https://doi.org/10.1017/S0022112000008661

Washburn, E.W., 1921. The Dynamics of Capillary Flow. Physical Review 17, 273–283. https://doi.org/10.1103/PhysRev.17.273

Weber, A.P., Friedlander, S.K., 1997. Relation between coordination number and fractal dimension of aerosol agglomerates. J. Aerosol Sci 28. https://doi.org/10.1016/S0021-8502(97)85381-5

Williams, J.J.E., Crane, R.I., 1983. Particle collision rate in turbulent flow. International Journal of Multiphase Flow 9, 421–435. https://doi.org/10.1016/0301-9322(83)90098-8

Witte, J., Hua, Z.C., Kolck, V., Kruggel-Emden, H., Heinrich, S., Schmidt, E., 2023. Investigation of a jet-based direct mixing process for improved structuring of conductive battery hetero-agglomerates. Processes 11. https://doi.org/10.3390/pr11113243

Witte, J., Kolck, V., Kruggel-Emden, H., Schmidt, E., 2025. Experimental Parameter Study of the Factors Influencing Dry Dispersion Using Laser Diffraction. Chemie Ingenieur Technik. https://doi.org/10.1002/cite.70039

Zaripov, D., Li, R., Dushin, N., 2019. Dissipation rate estimation in the turbulent boundary layer using high-speed planar particle image velocimetry. Exp. Fluids 60, 18. https://doi.org/10.1007/s00348-018-2663-4

Zhao, B., Su, Y., 2018. Particle size cut performance of aerodynamic cyclone separators: Generalized modeling and characterization by correlating global cyclone dimensions. J. Aerosol Sci. 120, 1–11. https://doi.org/10.1016/j.jaerosci.2018.02.009

Zhou, Y., Wexler, A.S., Wang, L.-P., 2001. Modelling turbulent collision of bidisperse inertial particles. J. Fluid Mech. 433, 77–104. https://doi.org/10.1017/S0022112000003372

Appendix

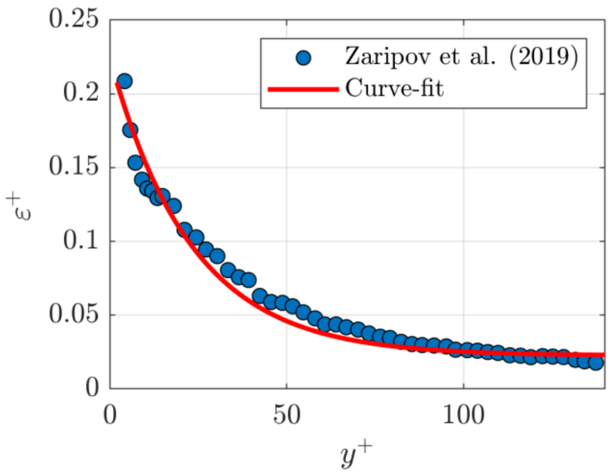

Fig. A1 Curve-fit of the non-dimensional turbulent energy dissipation rate ε^+ over the non-dimensional wall distance y^+ (Eq. (5)) in comparison with the experimental data from (Zaripov et al., 2019).

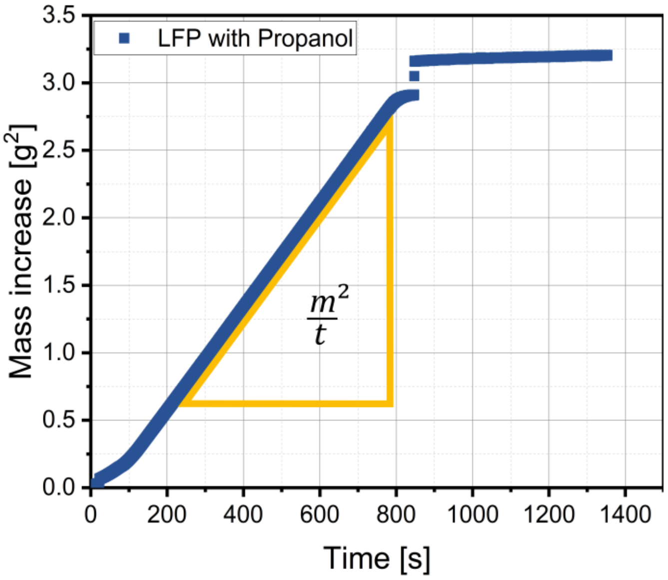

Fig. A2 Example of mass uptake measured with the Washburn device using LFP powder and propanol as the penetrating liquid.